nature communications

Article

https://doi.org/10.1038/s41467-026-71588-5

Industrial-level co-electrosynthesis of alkenol and $Mg(OH)_2$ from seawater over Nd_1Gd_1 dual atomic site on metallene

Received: 27 August 2025

Accepted: 25 March 2026

Published online: 15 April 2026

Check for updates

Qiqi Mao[1,2,4], Wenxin Wang[1,4], Ruidong Yang[1], Kai Deng[1], Hongjie Yu[1], Wenzhen Li[2] ✉, Liang Wang[1] ✉, Hongjing Wang[1] ✉ & Shaojun Guo[3] ✉

Industrial-level alkynols electrocatalytic semi-hydrogenation using seawater as hydrogen source offers a sustainable alternative to conventional thermocatalytic routes, yet remains limited by the lack of efficient and robust electrocatalysts. Here, we report the synthesis of Nd_1Gd_1 dual atomic site on metallene for co-production of alkenol and magnesium hydroxide in the seawater system. Nd_1Gd_1Pd metallene achieves a selectivity of ≈96.7% and a Faradaic efficiency of ≈87.3% for the conversion of 2-methyl-3-butyn-2-ol to 2-methyl-3-buten-2-ol at −150 mA cm^{-2} in a flow-cell system, and maintains ≈98.0% selectivity at 1.2 A for over 300 h of continuous operation, achieving the long-term stable co-electrosynthesis of alkenols and magnesium hydroxide in natural seawater at industrial-scale currents. Techno-economic analysis reveals a projected product revenue of at least $8,499 *per* ton of 2-methyl-3-buten-2-ol, underlining the industrial viability of this process. Mechanism investigations illustrate dual hydrogen-spillover and co-catalytic effects on Nd_1Gd_1Pd, promoting migration-reaction coupling mechanism of reactive *H to synergize hydrogenation. This work provides a seawater electrocatalytic semi-hydrogenation system and proposes an optimization strategy by atomically engineered dual hydrogen-spillover effect.

Alkenols are key intermediates in fine chemicals and bioscientific materials (e.g., vitamins, medicines, and perfumes)[1,2]. Among them, 2-methyl-3-buten-2-ol ($C_5H_{10}O$, MBE) is primarily used to synthesize the key intermediate isoamyl alcohol of vitamin E[3]. In conventional industry (Fig. 1a), MBE is produced by thermocatalytic hydrogenation of 2-methyl-3-butyn-2-ol (C_5H_8O, MBY) under high-temperature (≈300 °C) and high-pressure conditions (≈5 MPa), utilizing H_2 as the hydrogen source and Lindlar Pd catalysts, causing energy, safety and environmental issues[4,5]. In this regard, at ambient conditions, alkynol electrocatalytic semi-hydrogenation (ECSH) (Supplementary Fig. 1), which utilizes H_2O as a hydrogen source and drives the hydrogenation reaction to synthesize alkenol through an applied electric field[6], has aroused a widespread research interest as an emerging green catalytic pathway[7,8]. Currently, research on alkynol ECSH was usually done in alkaline freshwater systems (e.g., KOH or NaOH solutions)[9]. However, the expensive cost of alkaline media and the limited availability of freshwater resources further hamper the application prospects in large-scale industry[10,11]. Resource-rich seawater as a hydrogen source can significantly reduce freshwater consumption[12]. Moreover, seawater is naturally rich in alkaline ions (e.g., Na^+, Mg^{2+}, and Ca^{2+}) and anions (e.g., Cl^-, SO_4^{2-}), providing a natural electrolyte system for the electrocatalytic hydrogenation reaction to reduce the demand for additional alkaline media[13–15]. More notably, in the cathode reaction, the high concentration of Mg^{2+} in seawater can combine with OH^-

[1]State Key Laboratory of Green Chemical Synthesis and Conversion, Zhejiang Key Laboratory of Surface and Interface Science and Engineering for Catalysts, College of Chemical Engineering, Zhejiang University of Technology, Hangzhou, PR China. [2]Department of Chemical and Biological Engineering, Iowa State University, Ames, IA, USA. [3]School of Materials Science and Engineering, Peking University, Beijing, PR China. [4]These authors contributed equally: Qiqi Mao, Wenxin Wang. ✉e-mail: wzli@iastate.edu; wangliang@zjut.edu.cn; hjw@zjut.edu.cn; guosj@pku.edu.cn

https://doi.org/10.1038/s41467-026-71588-5

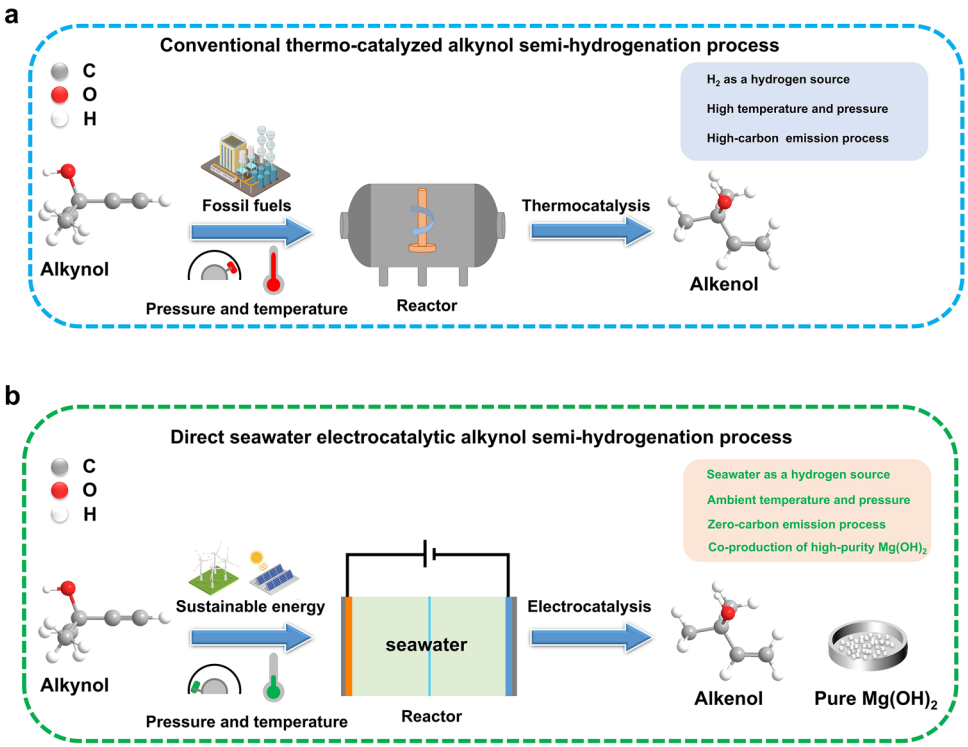

Fig. 1 | Schematic illustration of alkenol production pathways. Schematic illustration for alkenol production of (**a**) conventional industrial thermocatalytic alkynol semi-hydrogenation pathway and **b** proposed direct seawater electrocatalytic alkynol semi-hydrogenation pathway.

produced from the electrolysis process to form $Mg(OH)_2$[16,17]. $Mg(OH)_2$, a value-added functional material, finds widespread use across flame retardant systems, water purification, and bio-compatible applications[17]. Yet, its conventional synthesis often requires harsh alkaline reagents, complex purification, and energy-intensive industrial processes[18]. Hence, the construction of direct seawater alkynol ECSH and simultaneous $Mg(OH)_2$ production system provides a feasible approach for the development of alkynol ECSH and green synthesis of $Mg(OH)_2$. (Fig. 1b). Despite these inherent advantages, practical application of seawater-based ECH on an industrial scale still faces numerous challenges, including rapid catalyst deactivation, competitive hydrogen evolution reaction (HER), and uncontrollable over-hydrogenation reactions[3,13,19]. Currently, Cu-based and Pd-based catalysts have been widely explored as promising candidates for alkynol hydrogenation reactions[20–22]. Although Cu-based catalysts have exhibited good alkenol selectivity[3,6], their poor chlorine corrosion resistance leads to rapid dissolution, surface restructuring, and irreversible activity degradation under industrial-level current and localized alkaline conditions[23,24], rendering them unsuitable for long-term operation in seawater systems. In contrast, Pd-based catalysts offer good corrosion resistance and structure stability[25,26]. However, most reported Pd-based systems still operate at relatively low current densities for alkynol ECSH[4,5], which is limited by over-hydrogenation behavior and excessive HER activity on Pd under high current conditions[8]. Given this, the design of efficient and stable catalysts is urgently required for the development of MBY ECSH of seawater systems in industrial-scale conditions.

Here, we report the synthesis of Nd_1Gd_1Pdene and construct a Nd_1Gd_1Pdene-based sustainable membrane electrode assembly (MEA) electrolysis system for co-electrosynthesis of alkenol and $Mg(OH)_2$ in natural seawater. In the seawater flow cell system with 1 MBY, Nd_1Gd_1Pdene shows a high selectivity (≈96.7%) and FE (≈87.3%) of MBY to MBE at −150 mA cm^{-2}, while continuously generating high-purity $Mg(OH)_2$ at the cathode. The constructed MEA electrolyzer (4 cm^2) can operate stably for >300 h at an industrial-scale current density of 300 mA cm^{-2}, with a high MBE selectivity of approximately 98.0%, presenting the long-term stability and practical feasibility. This represents the demonstration of long-term stable co-electrosynthesis of alkenols and $Mg(OH)_2$ in natural seawater at industrial-scale currents. The projected revenue per ton of MBE produced under this system is at least approximately $8499 as revealed by techno-economic analysis (TEA), and the system presents lower economic cost and higher revenue compared with the conventional alkaline system, further indicating the economic feasibility. Mechanism investigations reveal that the introduction of dual single-atom Nd/Gd (Nd_1Gd_1) sites induces the dual hydrogen-spillover effect and the synergistic co-catalytic effect, which modulates the adsorption behavior of reactive *H on the surface to synergize MBY hydrogenation, and optimizes the adsorption energy and reaction energy barriers to facilitate the MBE desorption. This work enables the co-electrosynthesis of alkenols and $Mg(OH)_2$ in a seawater system via an atomically engineered dual hydrogen-spillover effect strategy.

Results and discussion

The synthesis of the rare-earth DSAA Nd_1Gd_1Pd metallene (Nd_1Gd_1Pdene) is accomplished through a facile one-step solvothermal process (Supplementary Fig. 2), where the generated dimethylamine (DMA) from decomposition of N,N-dimethylformamide (DMF) can promote the growth of 2D nanosheet structure through a metal facet control[27]. Representative transmission electron microscopy (TEM) and scanning electron microscopy (SEM) images of Nd_1Gd_1Pdene visually reveal the nanosheet structure with a significant curvature at a lateral size exceeding hundreds of nanometers (Fig. 2a and Supplementary Fig. 3). The nanoscale thickness is further confirmed via the atomic force microscopy (AFM) technology, revealing the thickness of an individual nanosheet for Nd_1Gd_1Pdene to be approximately 1.45 nm, comparable to typically 6–8 atomic layers (Supplementary Fig. 4). Such 2D nanosheet structures with a larger lateral size can provide high atom utilization, wider interfacial region (solid-gas/solid-liquid), and more specific exposed surfaces, facilitating the intercontact of the

https://doi.org/10.1038/s41467-026-71588-5

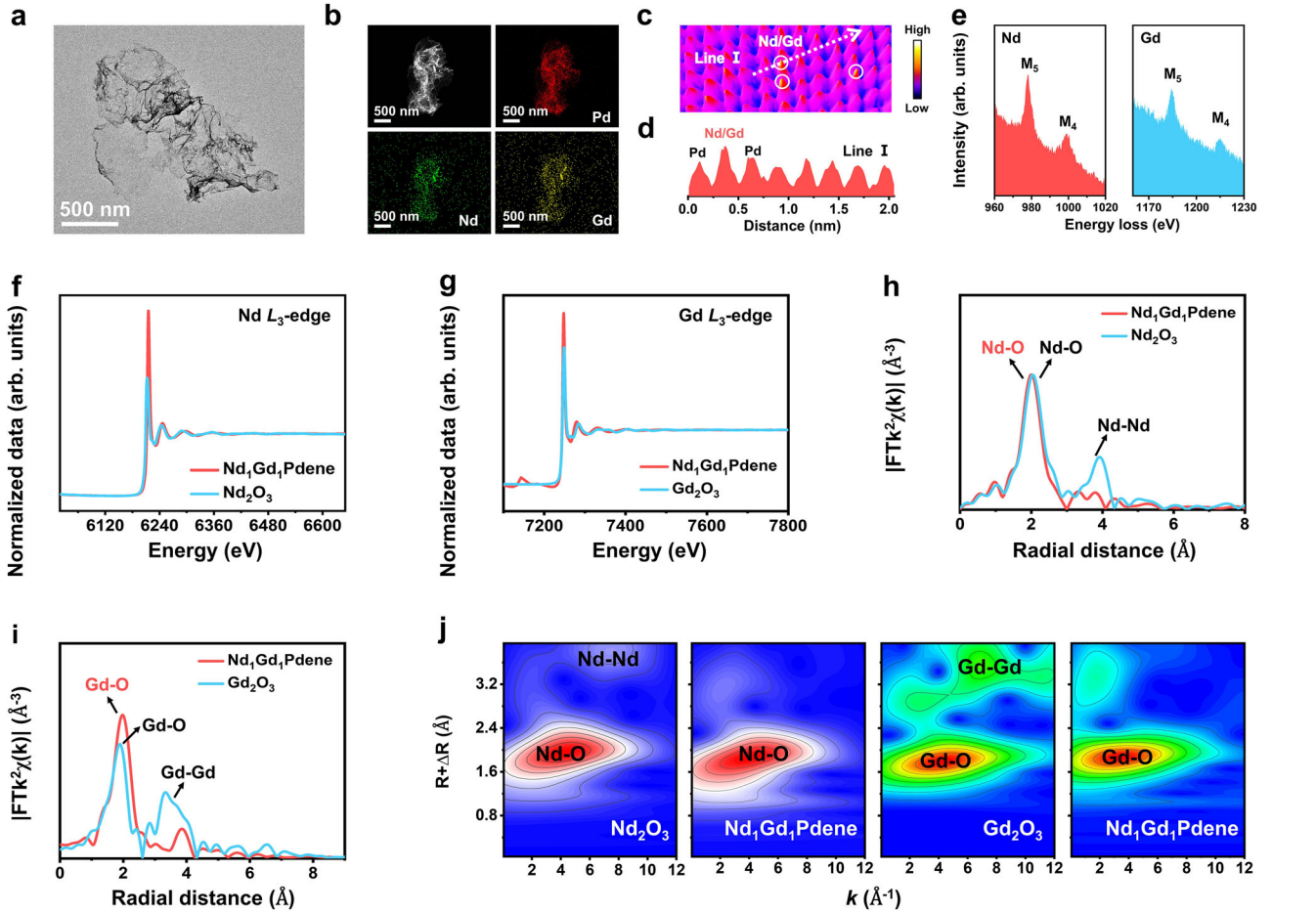

Fig. 2 | Structural and compositional characterization of Nd_1Gd_1Pdene catalyst. **a** TEM image, **b** HAADF-STEM and EDS elemental mapping images, and **c** 3D topographic atom image obtained from AC-HAADF-STEM for Nd_1Gd_1Pdene. **d** The atom intensity plot for line I in (**c**). **e** EELS spectra of Nd_1Gd_1Pdene. **f** Nd L_3-edge XANES spectra, **g** Gd L_3-edge XANES spectra, **h** Nd L_3-edge EXAFS spectra, **i** Gd L_3-edge EXAFS spectra and **j** wavelet transform spectra for Nd_1Gd_1Pdene, Nd_2O_3 and Gd_2O_3. *k* represents the photoelectron wave vector, and *R* denotes the radial distance in EXAFS analysis. Source data for the results are provided as a Source data file.

catalyst surface with the electrolyte/reactant and achieving fast charge transfer during the electrocatalytic reaction[27]. X-ray diffraction (XRD) patterns for Nd_1Gd_1Pdene and Pdene reveal the typical face-centered cube (fcc) structure of Pd (PDF#97-064-8676) (Supplementary Fig. 5), in which the diffraction peaks of Nd_1Gd_1Pdene exhibit no significant shift compared with Pdene and no pronounced peaks of Nd- and Gd-based structures are observed, implying the atomic dispersion of Nd and Gd without perturbation to the host crystal structure[28].

As shown in Fig. 2b, the combination of a high-angle annular dark field scanning transmission electron microscopy (HAADF-STEM) image and corresponding energy-dispersive X-ray spectroscopy (EDS) mappings reveals a uniform distribution of Pd, Nd, and Gd elements throughout the Nd_1Gd_1Pdene. Moreover, the SEM-EDS results of Nd_1Gd_1Pdene indicate the atomic ratio and mass ratio of Pd/Nd/Gd = 80.6%/9.0%/10.4% and Pd/Nd/Gd = 74.5%/11.3%/14.2% for Pd, Nd, and Gd, respectively (Supplementary Fig. 6), which is similar to the result for atomic ratio (Pd/Nd/Gd = 77.8%/10.5%/11.7%) and mass ratio (Pd/Nd/Gd = 70.7%/13.1%/16.2%) derived from inductively coupled plasma optical emission spectroscopy (ICP-OES) experiment (Supplementary Fig. 7).

False-color aberration-corrected HADDF-STEM (AC-HAADF-STEM) image of Nd_1Gd_1Pdene and the related fast Fourier transform (FFT) pattern reveal that the pattern displays a typical fcc structure as observed from the [011] diffraction zone and the lattice spacing of Nd_1Gd_1Pdene was measured to be 0.232 nm attributed to the Pd (111) crystal facet (Supplementary Fig. 8a), which is consistent with the XRD result. Notably, the well-organized polycrystalline nature of Nd_1Gd_1Pdene is observed and confirmed by selected-area electron diffraction (SAED) and the FFT pattern (inset in Supplementary Fig. 8a and Supplementary Fig. 9). 3D topographic atom images originated from AC-HAADF-STEM images and corresponding atomic intensity profile reveal several isolated high-intensity bright spots on Nd_1Gd_1Pdene (Fig. 2c, d, and Supplementary Fig. 8b), attributed to the Nd_1Gd_1 due to the higher atomic number of Nd and Gd (60/64) compared to the Pd (46). As revealed by the electron energy loss spectrum (EELS) in the selected region (Fig. 2e, Supplementary Figs. 10 and 11), the energy loss peaks around 998.8 and 978.1 eV can be ascribed to the $M_{4,5}$ transaction of Nd[29], and the energy loss peaks around 12,14.5 and 1184.6 eV can be ascribed to the $M_{4,5}$ transaction of Gd[30], indicating the presence of Nd_1Gd_1 detected at the atomic scale.

The chemical composition and surface valence state of Nd_1Gd_1Pdene were further investigated through X-ray photoelectron spectroscopy (XPS) tests (Supplementary Fig. 12). As shown in Supplementary Fig. 12b, the Pd 3*d* XPS spectrum of Nd_1Gd_1Pdene shows two obvious peaks situated at 340.4 (Pd $3d_{3/2}$) and 335.1 (Pd $3d_{5/2}$) eV, ascribed to the metallic state (Pd^0)[31], which indicates the predominant presence of Pd species in the metallic state. Simultaneously, two small peaks at 341.8 (Pd $3d_{3/2}$) and 336.5 (Pd $3d_{5/2}$) eV can be ascribed to the oxidation state (Pd^{2+})[32]. It is worth mentioning that the proportion of the oxidized state of Pd in Nd_1Gd_1Pdene is higher than that of Pdene,

which can arise from the slight ionization of Pd owing to the introduction of highly oxyphilic Nd_1Gd_1[33]. The peaks are located at 1004.3 (Nd $3d_{3/2}$), 997.5 (sat.), 981.7 (Nd $3d_{5/2}$) and 974.2 (sat.) eV, assigned to Nd^{3+} and satellite peaks[34], and also the peaks at 148.4 (Gd $4d_{3/2}$) and 142.7 (Gd $4d_{5/2}$) eV can be assigned to Gd^{3+} (Supplementary Fig. 12c, d)[30]. Notably, the binding energies of the peak positions (Nd 3*d* and Gd 4*d*) for Nd_1Gd_1Pdene present an obvious shift relative to those of Nd_2O_3 and Gd_2O_3, indicating the difference in the coordination environment of the Nd_1Gd_1 relative to those of Nd_2O_3 and Gd_2O_3[35].

To further reveal the electronic structure and atomic-level coordination environment of Nd_1Gd_1Pdene, X-ray adsorption spectroscopy technology was performed. The X-ray absorption near-edge structure (XANES) spectra of Nd L_3-edge and Gd L_3-edge for Nd_1Gd_1Pdene reveal that the absorption edges and white-line intensity peaks of Nd_1Gd_1Pdene are similar to those of Nd_2O_3 and Gd_2O_3, respectively (Fig. 2f, g), indicating the positively charged Nd_1Gd_1 in Nd_1Gd_1Pdene[36]. Furthermore, the white-line intensities of Nd_1Gd_1Pdene are higher than those of Nd_2O_3 and Gd_2O_3, further demonstrating the common electron transfer from Nd_1Gd_1 to Pd, hence resulting in the higher valence state induced by the more positive charge accumulation around the Nd_1Gd_1[37]. Figure 2h, i present the extended X-ray absorption fine structure (EXAFS) spectra of Nd L_3-edge and Gd L_3-edge for Nd_1Gd_1Pdene, Nd_2O_3 and Gd_2O_3. Compared with Nd_2O_3 and Gd_2O_3, the Nd_1Gd_1Pdene exhibits only one layer of Nd–O coordination (≈2.00 Å) and Gd–O coordination (≈1.98 Å) without Nd-Nd/Gd-Gd coordination, revealing that Nd/Gd is not coordinated with other Nd/Gd centers to exist as mutually isolated single-atom in Nd_1Gd_1Pdene, and further demonstrating that the coordination environment of the dual monatomic Nd/Gd in Nd_1Gd_1Pdene is different from that of Nd_2O_3 and Gd_2O_3, matching the XPS results.

As displayed in Fig. 2j, the wavelet transform (WT) spectra of Nd_1Gd_1Pdene indicate the intensity maximum exhibited at ≈4.11 and ≈3.44 $Å^{-1}$, respectively, ascribed to the Nd–O and Gd–O paths. Notably, it can be observed that the second intensity peaks (≈2.91 and ≈1.70 $Å^{-1}$) in WT spectra of Nd_1Gd_1Pdene are completely different from those in Nd_2O_3 and Gd_2O_3 (Nd-Nd: ≈7.48 $Å^{-1}$ and Gd-Gd: ≈6.98 $Å^{-1}$), which is probably reasonable that the second intensity peaks in the WT spectra of Nd_1Gd_1Pdene are attributed to the Nd-Pd and Gd-Pd paths, respectively. Besides, the high intensity of the Nd–O and Gd–O bonds can be ascribed to the highly oxyphilic nature of rare-earth elements, which induces inevitable oxidation of the rare-earth DSAA catalysts during the non-in situ tests[35]. The experimental and fitted EXAFS results for the Nd L_3-edge and Gd L_3-edge of Nd_1Gd_1Pdene, Nd_2O_3, and Gd_2O_3 demonstrate the favorable and appropriate fit values (Supplementary Figs. 13–16 and Supplementary Table 1). Encouragingly, comparison samples (Nd_1Pdene and Gd_1Pdene) were successfully prepared via this universal rare-earth SAA metallene synthesis method (Supplementary Figs. 17–19). Besides, Pdene was also synthesized for comparison (Supplementary Fig. 20).

In a direct seawater (from the Yellow Sea after sediment removal, Supplementary Table 2) system, the performance of ECSH of alkynol to alkenol and simultaneous production of magnesium hydroxide ($Mg(OH)_2$) on Nd_1Gd_1Pdene was investigated in a three-electrode system with a MEA-equipped flow cell under ambient conditions (Supplementary Fig. 21)[38]. An optimized MEA-equipped flow cell is beneficial for collecting the formed $Mg(OH)_2$ and avoiding the formation of precipitates occupying the active sites of the catalyst. Linear sweep voltammetry curves of Nd_1Gd_1Pdene visually show a significant decrease in cathode current density within the potential range of −1.2 ~ −2.4 V vs. Hg/HgO after the addition of MBY into seawater (Supplementary Fig. 22), indicating the electrocatalytic response of Nd_1Gd_1Pdene towards MBY semi-hydrogenation as well as the effective inhibition of the HER process by the MBY process on Nd_1Gd_1Pdene.

As revealed in Fig. 3a, the high MBE selectivity (>94.5%) is maintained on Nd_1Gd_1Pdene at various current densities (from −20 to −200 mA cm^{-2}). The highest MBE selectivity of ≈96.9% on Nd_1Gd_1Pdene is achieved at a current density of −50 mA cm^{-2}. The highest MBE production rate (r_{MBE}) of 5.2 mmol h^{-1} $mg_{cat.}^{-1}$ and high MBE selectivity of 96.7% are achieved on Nd_1Gd_1Pdene at a higher applied current density of −150 mA cm^{-2}, revealing the high selectivity and activity for MBY ECSH to MBE on Nd_1Gd_1Pdene using seawater as a hydrogen source, and the over-hydrogenation of MBE on Nd_1Gd_1Pdene is well suppressed at high current densities. Notably, the slight decrease in r_{MBE} (4.5 mmol h^{-1} $mg_{cat.}^{-1}$) for Nd_1Gd_1Pdene at −200 mA cm^{-2} originates from the enhanced competition reaction HER. The MBE FEs on Nd_1Gd_1Pdene approach ≈90.0% at current densities ranging from −20 to −150 mA cm^{-2}, and the MBE FE on Nd_1Gd_1Pdene reaches ≈99.7% at a current density of −50 mA cm^{-2}, with a catalytic partial current density for MBE production (j_{MBE}) of −49.9 mA cm^{-2} (Fig. 3b), indicating the high electron utilization efficiency for MBY to MBE on Nd_1Gd_1Pdene. A current density of −50 mA cm^{-2} can be used as a typical current density to investigate the time-dependent MBY conversion and MBE/2-methyl-2-butanol ($C_5H_{12}O$, MBA) yield over Nd_1Gd_1Pdene in seawater + 1 M MBY solution. It is obvious that MBY is gradually semi-hydrogenated to MBE with time and that the yield of the over-hydrogenation by-product MBA is minimal (Fig. 3c), revealing that the formed MBE at Nd_1Gd_1Pdene favors desorption rather than proceeding to an over-hydrogenation reaction during the MBY hydrogenation process. Supplementary Fig. 23 demonstrates that Nd_1Gd_1Pdene consistently holds the high selectivity (>95.0%) and FEs (≈99.0%) of MBE at different times, and the GC spectrum of MBY conversion of ≈98.8% further visually illustrates the high MBE selectivity on Nd_1Gd_1Pdene (Supplementary Fig. 24). Moreover, in contrast to GC tests, nuclear magnetic resonance (NMR) tests can be used as a complementary technology to investigate the products in the electrolyte directly. ^1H NMR and ^{13}C NMR spectra of the electrolyte after MBY ECSH (≈98.8% MBY conversion) on Nd_1Gd_1Pdene directly reveal the generation of MBE as well as low amounts of the by-products MBA and the reactant MBY (Supplementary Fig. 25), in line with the GC results.

To further investigate the stability and durability of co-production of MBE and $Mg(OH)_2$ on Nd_1Gd_1Pdene in a three-electrode seawater system, we performed the long-term (>500 h) chronopotentiometry (v–t) testing (Fig. 3d). Random spotting during stability testing indicates that Nd_1Gd_1Pdene retains stable performance of MBY ECSH to MBE in the direct seawater at −50 mA cm^{-2} (MBE Sel. > 95.0%, MBE FE > 96.0%). As presented in Supplementary Table 3, Nd_1Gd_1Pdene presents robust electrocatalytic performance for the constructed MBY ECSH to MBE system in direct seawater, which is competitive with the current Pd-based MBY ECSH electrocatalysts.

Moreover, these results also indirectly reveal that the electrocatalytic performance for MBY to MBE on Nd_1Gd_1Pdene is not affected by the generated $Mg(OH)_2$ precipitation (step I: $H_2O \rightarrow {}^*H + 2OH^-$; step II: MBY + 2*H → MBE; $Mg^{2+} + 2OH^- \rightarrow Mg(OH)_2$) during the MBY hydrogenation process. The pH of the electrolyte around the electrode was simulated and calculated using COMSOL to further analyze the generation of $Mg(OH)_2$ (Fig. 3e, f). The surface pH increases rapidly to ≈9.3 and remains stable at ≈10.0 within 5 min at a current of −50 mA cm^{-2}. These pH values fulfill the requirements for the precipitation of Mg^{2+} (≈9.3), but not for the precipitation of Ca^{2+} (≈12.0), resulting in the in situ formation of high-purity $Mg(OH)_2$ during the electrocatalytic hydrogenation process, and the produced trace Ca^{2+} precipitates are converted to $Mg(OH)_2$ via a complex decomposition reaction ($Mg^{2+} + Ca(OH)_2 \rightarrow Mg(OH)_2 + Ca^{2+}$)[16,17]. Moreover, we experimentally monitored the time-dependent actual pH changes of the catholyte during the MBY ECSH process in a seawater system. Supplementary Fig. 26 indicates that the pH value on the catalyst surface gradually increases initially and subsequently stabilizes at pH ≈ 9.8–10.0 without significant variation, which is consistent with the COMSOL simulation results, confirming that the local alkalization drives the selective formation of high-purity $Mg(OH)_2$.

https://doi.org/10.1038/s41467-026-71588-5

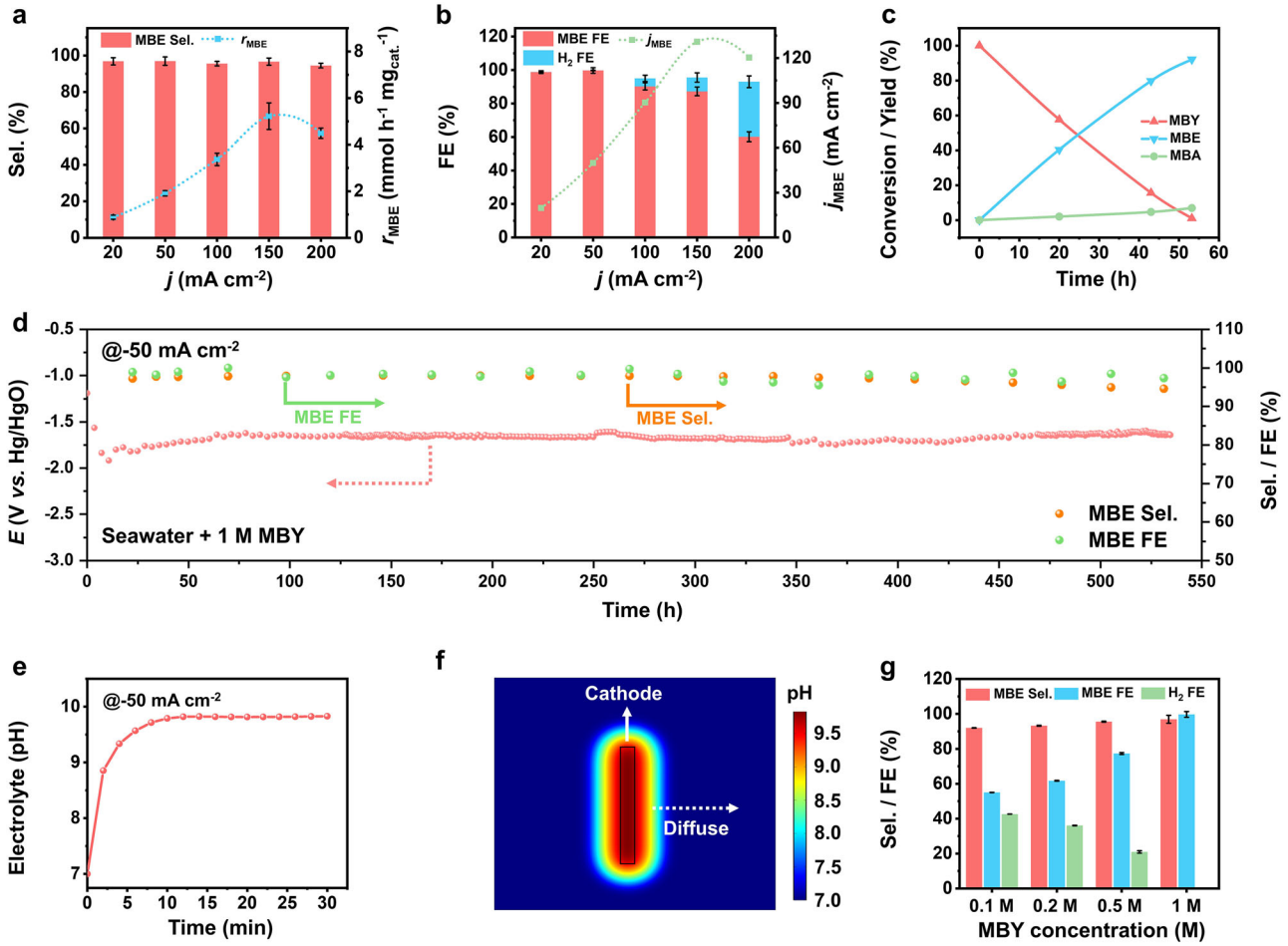

Fig. 3 | Performance of alkynol electrocatalytic semi-hydrogenation in seawater system. a MBE selectivity and r_{MBE} and **b** MBE/H_2 FE and j_{MBE} on Nd_1Gd_1Pdene at various applied current densities in a seawater containing 1 M MBY solution (pH = 7.85 ± 0.02, resistance: 3.25 ± 0.5 Ω) at 25 °C. **c** Time-dependent conversion/yield of MBY, MBE and MBA on Nd_1Gd_1Pdene at a current density of −50 mA cm^{-2} in a seawater containing 1 M MBY solution (pH = 7.85 ± 0.02, resistance: 3.25 ± 0.5 Ω) at 25 °C. **d** Stability test and MBE FE/selectivity on Nd_1Gd_1Pdene by the *υ*–*t* testing at a current density of −50 mA cm^{-2} in seawater containing 1 M MBY solutions (pH = 7.85 ± 0.02, resistance: 3.25 ± 0.5 Ω) at 25 °C. **e**, **f** COMSOL model of the pH distribution around the cathodic electrode at −50 mA cm^{-2} (area: 1 × 1 cm^2). **g** MBE selectivity, MBE FE and H_2 FE on Nd_1Gd_1Pdene at −50 mA cm^{-2} in seawater solutions with different MBY concentrations (pH = 7.85 ± 0.02, resistance: 3.25 ± 0.5 Ω) at 25 °C. Error bars display the standard deviation calculated from at least three independent measurements. The potentials were not iR-corrected. MBY 2-methyl-3-butyn-2-ol, C_5H_8O, MBE 2-methyl-3-buten-2-ol, $C_5H_{10}O$, MBA 2-methyl-2-butanol, $C_5H_{12}O$, Sel. selectivity, FE faradaic efficiency, r_{MBE} MBE production rate, *j* current density, j_{MBE} partial current density of MBE, *E* potential. Source data for the results are provided as a Source data file.

As shown in Fig. 3g, the effect of different MBY concentrations on the performance of MBY ECSH to MBE over Nd_1Gd_1Pdene in seawater was investigated. Observably, Nd_1Gd_1Pdene maintains the high MBE selectivity (>92.0%) at different MBY concentrations, even at a low MBY concentration, the Nd_1Gd_1Pdene also keeps high selective hydrogenation for MBY to MBE, implying that the alteration of MBY concentration has almost no effect on the MBE selectivity on Nd_1Gd_1Pdene. Notably, the MBE FE of Nd_1Gd_1Pdene gradually increases as MBY concentration is increased, which can originate from the fact that the increase of local MBY concentration around the catalyst promotes the stronger adsorption of MBY on the catalyst surface, contributing to the inhibition of the competing reaction HER[3]. Besides, considering that the electrolyte is a mixed solution containing the inorganic electrolyte and organic, the further increase of reactant concentration can lead to a reduction of conductivity to affect the reaction efficiency in MBY ECSH on Nd_1Gd_1Pdene, hence the reactant concentration is not further expanded (<1 M)[3].

Supplementary Fig. 27 further shows the effect of different electrolyte concentrations on the performance of MBY ECSH over Nd_1Gd_1Pdene in simulated seawater. Apparently, Nd_1Gd_1Pdene exhibits the stable performance of MBE electrosynthesis at different NaCl concentrations, which indicates that there is almost no effect of major inorganic Na^+ and Cl^- in seawater on the cathodic electrocatalytic MBY semi-hydrogenation process on Nd_1Gd_1Pdene. Moreover, we also investigated the performance of MBE ECSH to MBE over Nd_1Gd_1Pdene under different pH conditions (Supplementary Fig. 28). Similar to the performance under neutral conditions in seawater, Nd_1Gd_1Pdene also exhibits the activity (MBE selectivity: ≈97.9%, MBE FE: ≈97.0%) of MBY ECSH to MBE under alkaline conditions.

A series of comparison experiments were carried out to further investigate the effect of the Nd_1Gd_1. Nd_1Gd_1Pdene possesses the highest MBE selectivity and r_{MBE} (−100 mA cm^{-2}: ≈95.6%, ≈3.4 mmol h^{-1} mg$_{cat.}^{-1}$; −200 mA cm^{-2}: ≈94.5%, ≈4.5 mmol h^{-1} mg$_{cat.}^{-1}$) compared to those of Nd_1Pdene (−100 mA cm^{-2}: ≈89.4%, ≈2.2 mmol h^{-1} mg$_{cat.}^{-1}$; −200 mA cm^{-2}: ≈93.5%, ≈0.8 mmol h^{-1} mg$_{cat.}^{-1}$), Gd_1Pdene (−100 mA cm^{-2}: ≈95.2%, ≈3.0 mmol h^{-1} mg$_{cat.}^{-1}$; −200 mA cm^{-2}: ≈85.0%, ≈1.2 mmol h^{-1} mg$_{cat.}^{-1}$) and Pdene (−100 mA cm^{-2}: ≈94.7%, ≈2.9 mmol h^{-1} mg$_{cat.}^{-1}$; −200 mA cm^{-2}: ≈90.3%, ≈2.8 mmol h^{-1} mg$_{cat.}^{-1}$) (Supplementary Fig. 29a, b), indicating the improvement of MBE selectivity and r_{MBE} on Nd_1Gd_1Pdene due to the synergistic effect of

https://doi.org/10.1038/s41467-026-71588-5

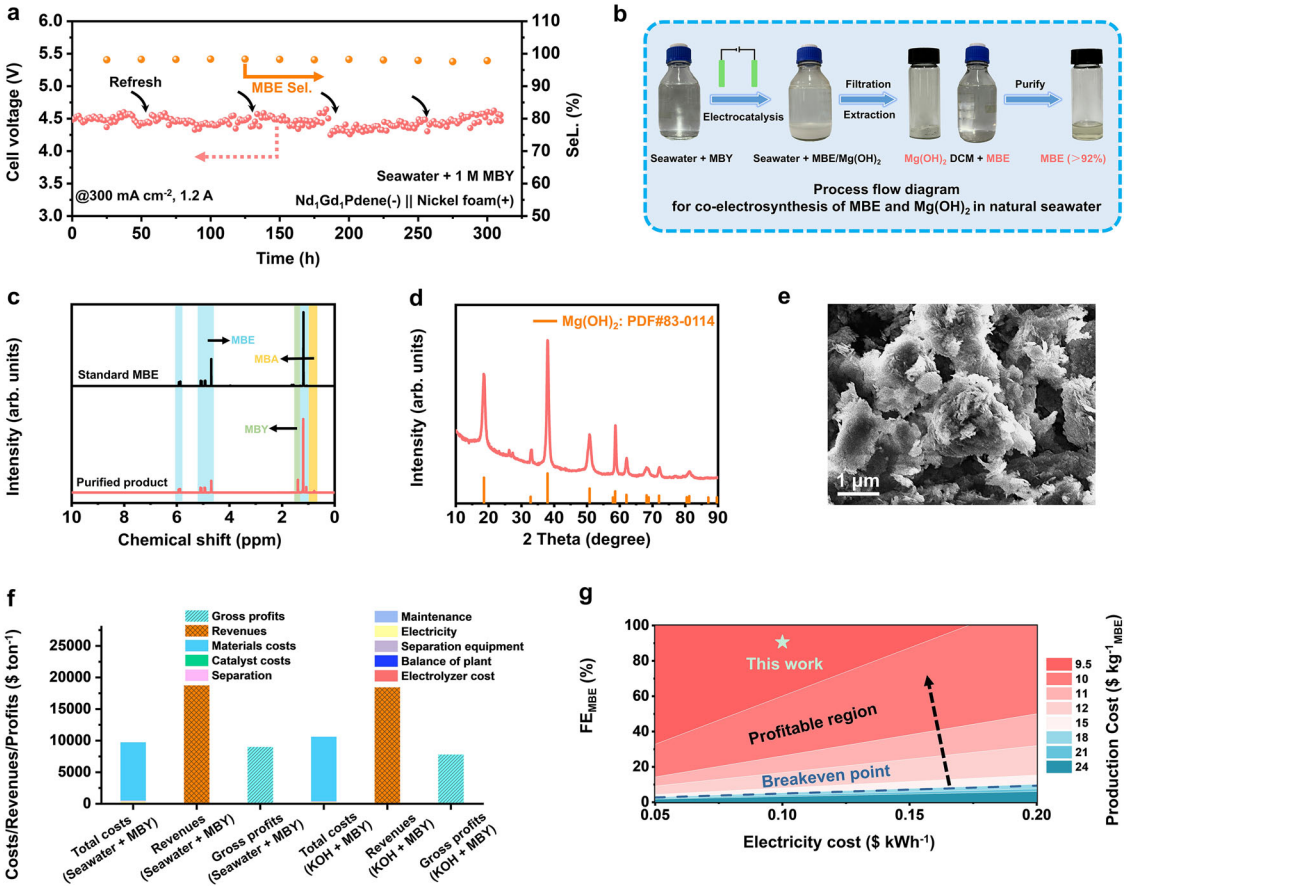

Fig. 4 | Performance and techno-economic analysis (TEA) of seawater alkynol electrocatalytic semi-hydrogenation. a Durability test and MBE selectivity of continuous 300 h electrolysis on Nd_1Gd_1Pdene in an optimized 4-cm^2 MEA electrolyzer at a constant industrial-scale current density of 300 mA cm^{-2} in seawater containing 1 M MBY solutions (cathode: pH = 7.85 ± 0.02; cell resistance: 3.9 ± 0.2 Ω) at 25 °C. **b** Scheme of the process flow for MBY ECSH to MBE and electrochemical extraction of $Mg(OH)_2$ in direct seawater. **c** ^{1}H NMR spectra of MBE purified from 300-h post-reaction electrolyte and corresponding standard MBE. **d** XRD pattern and **e** SEM image of $Mg(OH)_2$ collected from 300-h post-reaction electrolyte. **f** Assessment of economic indicators for various alkenol electrosynthesis systems. **g** TEA results of proposed electrocatalytic alkenol synthesis and electrochemical extraction of $Mg(OH)_2$ from seawater at 0.1 A cm^{-2}. The potentials were not iR-corrected. MBY 2-methyl-3-butyn-2-ol, C_5H_8O, MBE 2-methyl-3-buten-2-ol, $C_5H_{10}O$, MBA 2-methyl-2-butanol, $C_5H_{12}O$, Sel. selectivity, FE faradaic efficiency. Source data for the results are provided as a Source data file.

Nd_1Gd_1. Notably, the r_{MBE}s of Nd_1Pdene and Gd_1Pdene decrease significantly at an increasing current density, which probably stems from the facilitation of the HER process by the introduction of a single rare-earth metal at a high current density. This point is proven by comparing the FE of the samples at different current densities (Supplementary Fig. 29c, d). Nd_1Gd_1Pdene possesses a higher MBE FE (≈90.3%, ≈60.2%) compared to the other comparison samples (Nd_1Pdene: ≈59.5%, ≈10.6%, Gd_1Pdene: ≈79.1%, ≈16.4%, Pdene: ≈78.5%, ≈38.0%).

To further investigate the potential for practical application of continuous co-production of MBE and $Mg(OH)_2$ on Nd_1Gd_1Pdene in a seawater system, the electrochemical activity and stability of Nd_1Gd_1Pdene were investigated using an optimized MEA electrolyzer (4 cm^2) at an industrial level current density (300 mA cm^{-2}, 1.2 A) (Fig. 4a and Supplementary Fig. 30), and the produced $Mg(OH)_2$ produced was collected during the process. Figure 4a shows that Nd_1Gd_1Pdene delivers the stability of at least 300 h in the MEA cell with consistently high MBE selectivity (98.0%) and an MBE production rate of 2.15 mmol h^{-1} cm^{-2} in the seawater system at a current density of 300 mA cm^{-2}. Notably, no dramatic over-hydrogenation behavior was observed due to the strong current of 1.2 A. This reveals the practical potential for targeted electrosynthesis of MBE at an industrial-scale current density. Although the CEM was employed to separate the anode and cathode to prevent interference from anodic OH^-, to further illustrate the feasibility and authenticity of co-electrosynthesis of alkenol and $Mg(OH)_2$ in the constructed MEA electrolyzer, the anode electrolyte KOH was replaced with natural seawater or Na_2SO_4 solutions while maintaining natural seawater as the cathode solution for continuous electrolysis. Owing to the irreversible corrosion and poisoning of anodic OER catalysts caused by ionic species in natural seawater, this may affect the long-term stability of the MEA electrolyzer. Therefore, we employed a Na_2SO_4 solution as a feasible alternative to natural seawater for the anode in long-term stability testing[15]. Supplementary Fig. 31 shows that the MEA electrolyzer system still maintains the catalytic activity and stability under these conditions. Also, the post-electrolysis morphology, structure, and chemical composition of Nd_1Gd_1Pdene were investigated. No significant degradation of the 2D nanosheet structure of Nd_1Gd_1Pdene is observed after the long-term device testing (Supplementary Fig. 32). Supplementary Fig. 33 shows that Nd_1Gd_1Pdene maintains a good crystalline structure, stable elemental compositions and surface chemical states after stability testing, indicating structural and compositional stability under prolonged electrolysis. Figure 4b presents a process flow diagram to obtain MBE and $Mg(OH)_2$ from the cathodic solution of the MEA electrolyzer by an electrocatalysis-separation-purification process, which typically involves three steps. Step 1: the electrolyte product and $Mg(OH)_2$ are obtained by electrocatalysis; step 2: the $Mg(OH)_2$

https://doi.org/10.1038/s41467-026-71588-5

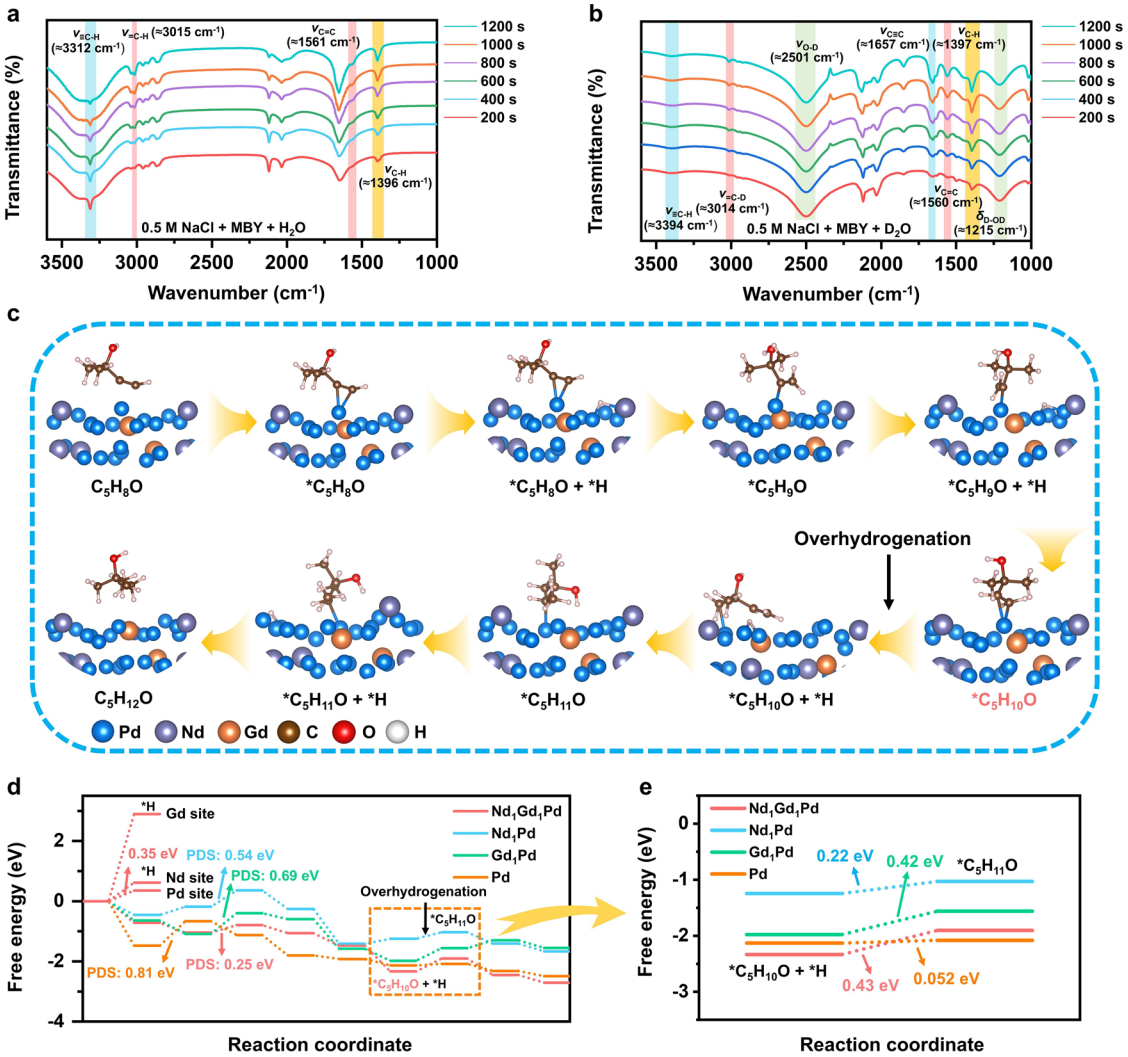

Fig. 5 | Mechanistic insights into alkynol electrocatalytic semi-hydrogenation. In situ FTIR spectra of MBY ECSH on Nd_1Gd_1Pdene at various time (from 200 to 1200 s) in (**a**) simulated seawater (0.5 M NaCl, H_2O as H source) + 1 M MBY (pH = 7.11 ± 0.02) and (**b**) simulated seawater (0.5 M NaCl, D_2O as D source) + 1 M MBY solutions (pD = 7.40 ± 0.02). **c** Optimized structures of MBY ECH intermediates on Nd_1Gd_1Pd model. **d** Comparison of free energy profiles of MBY ECH pathway on Nd_1Gd_1Pd, Nd_1Pd, Gd_1Pd and Pd models. **e** Enlarged free energy profiles in the orange block region of (**d**). PDS: potential-determining step. MBY 2-methyl-3-butyn-2-ol, C_5H_8O, MBE 2-methyl-3-buten-2-ol, $C_5H_{10}O$, MBA 2-methyl-2-butanol, $C_5H_{12}O$. Source data for the results are provided as a Source data file.

precipitation is firstly obtained by filtration/centrifugation, and then the centrifuge solution is extracted to obtain MBE, including the extracted solution; step 3: the high-purity MBE is obtained by a purification process (vacuum distillation). The NMR spectra of the obtained cathodic electrolyte product prove that high-purity MBE can be obtained by this electrocatalytic process flow (Fig. 4c and Supplementary Fig. 34). Moreover, the XRD spectra of $Mg(OH)_2$ collected by this process flow further show that only the diffraction peaks of $Mg(OH)_2$ can be observed without other inorganic precipitation peaks (Fig. 4d), which is in accordance with the results of COMSOL simulation. SEM image of $Mg(OH)_2$ indicates the uniform distribution for the nanoscale structure of $Mg(OH)_2$ (Fig. 4e). TEA of the constructed seawater MBY ECSH system shows that for every 1 ton of MBE produced in the system, the plant-gate levelized costs of ≈9739.2 $ are lower than the revenues (≈18,739.1 $) generated by the process (Fig. 4f, g). The constructed system presents a lower economic cost and higher revenue than the conventional alkaline MBY ECSH system.

Supplementary Fig. 35 and Supplementary Table 4 reveal that the obtained resistance (R_{ct}) value of Nd_1Gd_1Pdene (≈4.3 Ω) is much lower than the values of Nd_1Pdene (≈6.2 Ω), Gd_1Pdene (≈7.2 Ω), and Pdene (≈7.8 Ω), indicating a greater conductivity and faster interfacial charge transfer on Nd_1Gd_1Pdene due to the introduction of the dual monatomic Nd/Gd[39]. Moreover, the electrochemical active surface areas (ECSAs) of samples were evaluated through calculating the electrochemical double layer capacitance (C_{dl}) from cyclic voltammetry (CV) curves at various scan rates (20–120 mV s^{-1}) (Supplementary Fig. 36). Supplementary Fig. 37 shows that Nd_1Gd_1Pdene presents a higher C_{dl} value of ≈8.4 mF cm^{-2} compared to Nd_1Pdene (≈7.6 mF cm^{-2}), Gd_1Pdene (≈6.9 mF cm^{-2}) and Pdene (≈5.3 mF cm^{-2}), which reveals that the larger ECSA of Nd_1Gd_1Pdene can expose more active sites, thus improving the electrocatalytic activity[3].

Electrochemical in situ Fourier transform infrared (FTIR) tests were performed on Nd_1Gd_1Pdene to visually observe the changes of intermediates in the electrocatalytic MBY hydrogenation reaction. As presented in Fig. 5a, the vibration peaks observed at ≈3312 and ≈1396 cm^{-1} are attributed to $\nu_{\equiv C-H}$ and ν_{C-H} of MBY, respectively[5]. Furthermore, the vibration peaks at ≈3015 and ≈1561 cm^{-1} occur and gradually increase as electrolysis time extends, which can be assigned to $\nu_{=C-H}$ and $\nu_{C=C}$ of MBE, respectively[5,8], indicating the gradual conversion of adsorbed MBY to MBE on Nd_1Gd_1Pdene. However, it is

notable that after the addition of MBY, the H_2O peaks become excessively broad and overlaps with the $\nu_{\equiv C-H}$ and $\nu_{C\equiv C}$ peaks. In particular, the $\nu_{C\equiv C}$ peak is difficult to distinguish with the δ_{H-O-H} of H_2O (≈1650 cm^{-1}). To further accurately identify key species and determine the proton source, D_2O was employed as both the solvent and proton source. As displayed in Fig. 5b, the peaks of $\nu_{\equiv C-H}$ (≈3394 cm^{-1}), $\nu_{C\equiv C}$ (≈1657 cm^{-1}), ν_{C-H} (≈1397 cm^{-1}), $\nu_{=C-D}$ (≈3014 cm^{-1}) and $\nu_{C=C}$ (≈1657 cm^{-1}) are distinctly observable and similar to those observed with H_2O as the proton source, indicating the conversion of MBY (C_5H_8O) to MBE ($C_5H_{10}O$)/MBE-d_2 ($C_5H_8D_2O$) via H_2O/D_2O dissociation as the proton source on Nd_1Gd_1Pdene. The intensity of the $\nu_{C\equiv C}$ gradually increases as time extends, suggesting the adsorption of MBY on the Nd_1Gd_1Pdene surface. Notably, the vibration peak of $\nu_{C\equiv C}$ appears to be red-shifted compared to gaseous MBY, which indicates the tendency of MBY to form a di-σ/π-bonded configuration on the Nd_1Gd_1Pdene surface[40]. More importantly, no relevant vibration frequencies of the MBA are observed during the time-dependent hydrogenation process, further revealing the weak over-hydrogenation effect on Nd_1Gd_1Pdene, consistent with the experimental test results.

The MBY semi-hydrogenation mechanism on Nd_1Gd_1Pdene is further investigated by density functional theory (DFT) calculations. Supplementary Fig. 38 shows the optimized geometrical configuration for the Nd_1Gd_1Pdene catalyst. Figure 5c, d, and Supplementary Figs. 39–41 illustrate the MBY hydrogenation pathway on Nd_1Gd_1Pd through a reactive *H-mediated process using water as the hydrogen source. Observably, the hydrogenation process of $C_5H_8O^* + {}^*H$ to $C_5H_9O^*$ on Nd_1Gd_1Pd surface presents a lower energy barrier ($\Delta G = 0.25$ eV) compared with the desorption process of *H (2*H → H_2, 0.35 eV) (Fig. 5d), indicating a higher MBY activity on Nd_1Gd_1Pd compared to HER. In the hydrogenation of MBY to MBE, the energy barrier ($\Delta G = 0.25$ eV) of Nd_1Gd_1Pd for the potential-determining step is lower than those of Nd_1Pd ($\Delta G = 0.54$ eV), Gd_1Pd ($\Delta G = 0.69$ eV), and Pd ($\Delta G = 0.81$ eV) (Fig. 5d and Supplementary Table 5), suggesting a higher electrocatalytic activity for the conversion of MBY to MBE on Nd_1Gd_1Pd. Compared with Nd_1Pd ($\Delta G = 0.22$ eV), Gd_1Pd ($\Delta G = 0.42$ eV), and Pd ($\Delta G = 0.052$ eV) (Fig. 5e and Supplementary Table 5), Nd_1Gd_1Pd requires a higher energy barrier ($\Delta G = 0.43$ eV) for the step of MBE over-hydrogenation to alkanols (*MBE → *MBA), indicating a weak over-hydrogenation effect on Nd_1Gd_1Pd. Furthermore, Supplementary Fig. 42 and Supplementary Table 6 show that the MBE adsorption energy ($\Delta E_{ads} = -0.93$ eV) of Nd_1Gd_1Pd is weaker than those of Nd_1Pd ($\Delta E_{ads} = -1.08$ eV), Gd_1Pd ($\Delta E_{ads} = -1.06$ eV), and Pd ($\Delta E_{ads} = -1.14$ eV), contributing to the high MBE selectivity on Nd_1Gd_1Pd. This can originate from that the introduced Nd_1Gd_1 increases the charge density on the Pd host surface, favoring weakening the adsorption capacity of the C=C groups.

The electronic structure changes on Nd_1Gd_1Pd are further analyzed by the Bader charge and differential charge density (Supplementary Figs. 43 and 44). The total Bader charges for Pd, Nd and Gd are 14.65, −7.22 and −7.43 e in the Nd_1Gd_1Pd model (Supplementary Table 7), respectively, suggesting that electron co-transfer from the Nd_1Gd_1 to the Pd host, thus leading to an electron-rich state of Pd, which is consistent with the XANES test results. As shown in Supplementary Fig. 45a and Supplementary Table 8, the projected density of states plots of Nd_1Gd_1Pd show a proper coupling effect close to the Fermi level (E_F) between the Pd-4*d* orbital energy bands and the Nd-4*f*/Gd-4*f* orbital energy bands, suggesting the existence of *d*-*f* orbital hybridization interaction in Nd_1Gd_1Pd. Due to the 4*f* electron configuration of rare-earth elements, this interaction is beneficial for optimizing the surface electron structure to accelerate charge transfer, thus improving the intrinsic activity of the catalysts in electrocatalytic reactions[35,41]. Compared with the *d*-band center of pure Pd (−1.93 eV), Nd_1Pd (−2.06 eV), and Gd_1Pd (−2.05 eV), the *d*-band center of Nd_1Gd_1Pd is −2.07 eV (Supplementary Fig. 45b and Supplementary Table 8), which presents a slightly downshift to the E_F. This electronic modulation weakens the adsorption strength of intermediates, thereby facilitating the desorption of the target product MBE from the Nd_1Gd_1Pd surface, consistent with MBE ΔE_{ads} results (Supplementary Fig. 42 and Supplementary Table 6), thus contributing to the enhanced selectivity toward MBY ECSH.

The investigation of changes in reactive *H species generated by the H_2O adsorption-dissociation is key to analyzing the efficient conversion of MBY semi-hydrogenation to MBE. Various experiments and theoretical simulations were carried out to monitor the behavior of H_2O and reactive *H on Nd_1Gd_1Pd. Since the appearance of *H characteristic peaks in the CV curves of the double layer region is directly related to the degree of H enrichment on the catalyst surface[6], the hydrogenation behavior of active *H was monitored by comparing the CV curves of Nd_1Gd_1Pd in 1 M NaOH with and without MBY (Fig. 6a). When MBY is not added into the electrolyte, Nd_1Gd_1Pd exhibits a strong desorption peak of adsorbed Pd-H species around −0.6 V vs. Hg/HgO. When MBY is added into the electrolyte, the desorption peak of Pd-H species for Nd_1Gd_1Pd almost disappears, which indicates that the generated reactive *H species on the surface are completely consumed and efficiently utilized in the MBY hydrogenation process.

Moreover, electron paramagnetic resonance (EPR) tests were performed using 5,5-dimethyl-1-pyrroline-N-oxide (DMPO) as the *H trapping reagent (Fig. 6b). In the electrocatalytic test without MBY, Nd_1Gd_1Pd exhibits a significant DMPO-H signal, indicating the ability of the Nd_1Gd_1Pd surface to generate reactive *H by H_2O dissociation. In the electrocatalytic test with MBY, Nd_1Gd_1Pd exhibits an almost undetectable DMPO-H signal, suggesting that the reactive *H produced by H_2O dissociation is rapidly consumed for MBY hydrogenation. Meanwhile, a series of control experiments was conducted to eliminate environmental factors interfering with DMPO trapping. Supplementary Fig. 46a, b indicates that no DMPO-H signal is detected in solutions with or without MBY in the absence of a catalyst and applied current, further illustrating that reactive *H formation originates from catalytic generation on Nd_1Gd_1Pd. Notably, when MBY and DMPO are simultaneously introduced into a 0.5 M NaCl solution after electrolysis, a pronounced DMPO-H signal is observed, indicating no interference from the reactant MBY in DMPO trapping (Supplementary Fig. 46c). These results further confirm that the disappearance of the DMPO-H signal in the presence of MBY originates from the *H consumption during the electrocatalytic hydrogenation process.

The in situ FTIR profiles of Nd_1Gd_1Pd indicate a slight vibration peak on Nd_1Gd_1Pd at a vibration frequency of ≈1992 cm^{-1} in 0.5 M NaCl + 1 M MBY + H_2O (Fig. 6c), which is ascribed to the vibration frequency of the Pd−H signal (ν_{Pd-H}) on the Nd_1Gd_1Pd surface[6], further revealing the formation of reactive *H during the dynamic process and the MBY ECSH process on Nd_1Gd_1Pd as a mechanism of the reactive *H-mediated hydrogenation reaction. Moreover, the relatively weak Pd−H signal on Nd_1Gd_1Pd can be attributed to the effect of the enhanced overtone or combination bands (≈2040 cm^{-1}) by Fermi resonance with a nearby fundamental mode in the presence of MBY[8], as well as rapid hydrogen consumption during MBY ECSH. This is further supported by the observation of pronounced Pd-H vibration peak in the absence of MBY (Supplementary Fig. 47), which demonstrates the strong H_2O dissociation ability of Nd_1Gd_1Pdene to generate reactive *H species. Notably, compared with the MBY ECSH, the significantly stronger Pd−H signal indicates a suppressed HER activity on Nd_1Gd_1Pdene, leading to the accumulation of *H, further supporting the more favorable MBY hydrogenation reaction on Nd_1Gd_1Pdene.

The electron-deficient Nd_1Gd_1 can serve as both Lewis acid sites to attract Lewis bases, and in neutral environments, H_2O generally behaves as a Lewis base due to the lone pair electrons of O (σ-donation)[41]. Under the neutral conditions of seawater, H_2O tends to adsorb more readily around the electron-deficient Nd_1Gd_1 sites,

https://doi.org/10.1038/s41467-026-71588-5

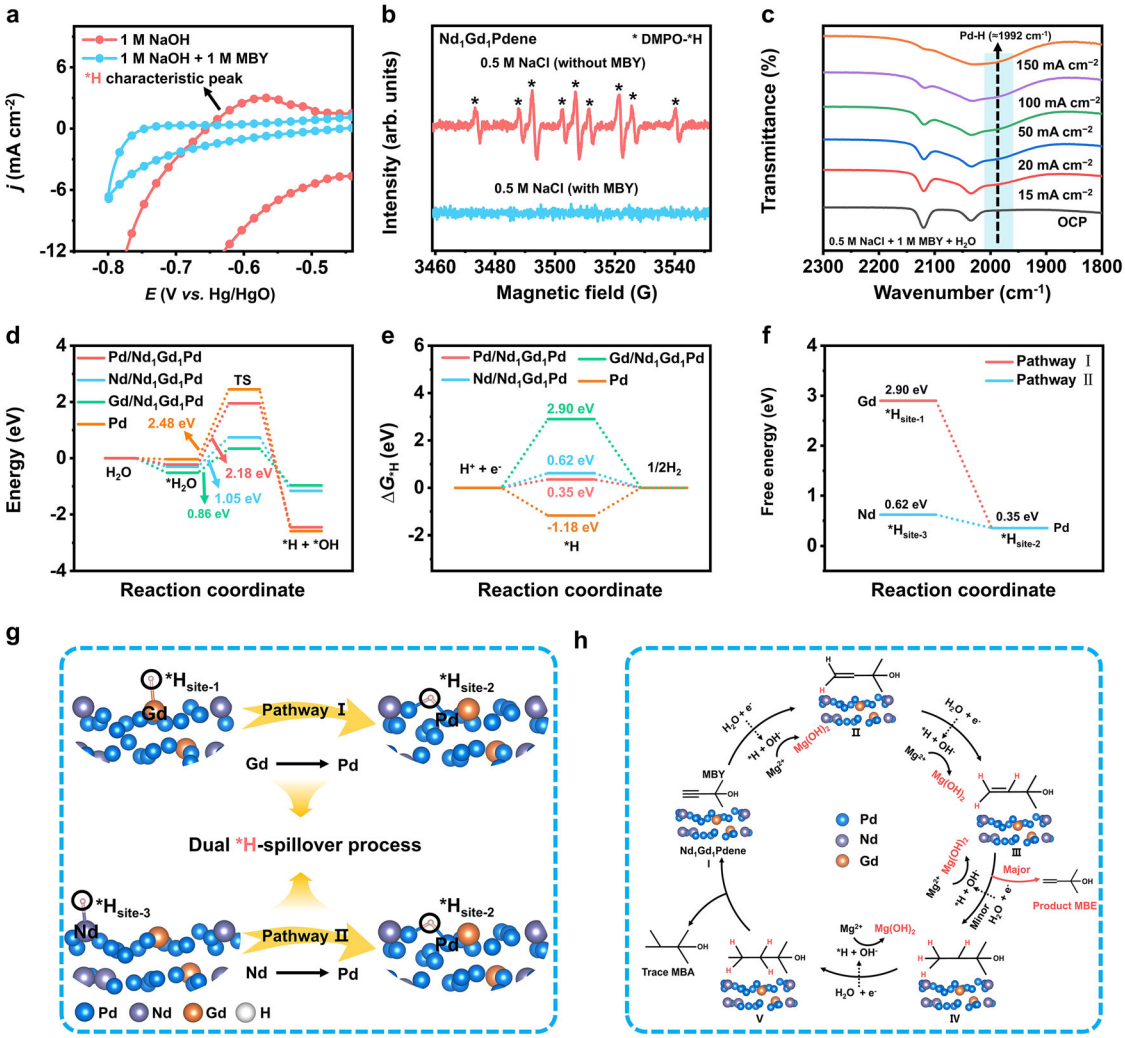

Fig. 6 | Mechanistic insights into reactive *H behavior during alkynol electrocatalytic semi-hydrogenation. a CV curves of Nd_1Gd_1Pdene at a scan rate of 50 mV s^{-1} in a 1 M NaOH solution with and without MBY (pH = 13.87 ± 0.02) at 25 °C. **b** DMPO-added EPR spectra of Nd_1Gd_1Pdene in a simulated seawater (0.5 M NaCl) with or without MBY (pH = 7.11 ± 0.02). **c** In situ FTIR spectra of MBY ECSH on Nd_1Gd_1Pdene at various current density in a simulated seawater (0.5 M NaCl, H_2O) + 1 M MBY solution (pH = 7.11 ± 0.02). Comparison of **d** H_2O dissociation energy barrier profiles and **e** hydrogen free energy profiles of HER for various sites (Pd, Nd, and Gd sites) of Nd_1Gd_1Pd and Pd. **f** Comparison of free energy profiles at different *H adsorption sites on Nd_1Gd_1Pd model. **g** Schematic diagram of dual single-atom site hydrogen spillover effect for different adsorbed *H sites of Nd_1Gd_1Pd model. **h** Plausible reaction mechanism for the co-electrosynthesis of MBE and $Mg(OH)_2$ in direct seawater. MBY 2-methyl-3-butyn-2-ol, C_5H_8O, MBE 2-methyl-3-buten-2-ol, $C_5H_{10}O$, MBA 2-methyl-2-butanol, $C_5H_{12}O$, DMPO 5,5-dimethyl-1-pyrroline-N-oxide, *j* current density, ΔG_{*H} hydrogen adsorption free energy. Source data for the results are provided as a Source data file.

resulting in the Nd_1Gd_1 sites acting as an effective H_2O adsorption site to further reduce the competition adsorption between the H_2O and MBY on the Pd host. Supplementary Fig. 48 and Supplementary Table 9 further show the adsorption energies (ΔE_{ads}) of H_2O on Nd_1Gd_1Pd with different sites (Pd: $\Delta E_{ads} = -0.23$ eV, Nd: $\Delta E_{ads} = -0.30$ eV, Gd: $\Delta E_{ads} = -0.52$ eV) and pure Pd (Pd: $\Delta E_{ads} = -0.04$ eV), suggesting that the introduction of Nd_1Gd_1 can serve as the main H_2O adsorption site and further enhance the reactant H_2O adsorption. Moreover, the electron-rich Pd favors the formation of strong interactions between Pd and the π-electron cloud of C≡C in MBY to enhance the adsorption of MBY[4]. The ΔE_{ads} of H_2O and MBY on Nd_1Gd_1Pd indicate the easier adsorption of MBY ($\Delta E_{ads} = -1.79$ eV) on Nd_1Gd_1Pd compared to H_2O ($\Delta E_{ads} = -0.52$ eV) (Supplementary Fig. 49 and Supplementary Table 10), suggesting a preferred electrocatalytic MBY hydrogenation process on Nd_1Gd_1Pd. More importantly, as the MBY concentration increases, the coverage of MBY on the Nd_1Gd_1Pd surface is expanded, which intrinsically hinders H_2O adsorption. At high MBY concentrations, HER kinetics are more strongly inhibited, thereby enhancing the FE of MBE, consistent with electrochemical experimental results[3].

Figure 6d, Supplementary Figs. 50, 51, and Supplementary Table 11 exhibit the optimized configurations and energy profiles of the initial, transition, and final states for the H_2O dissociation process on Nd_1Gd_1Pd with different sites and pure Pd, where the Nd_1Gd_1 sites on Nd_1Gd_1Pd possess the lower H_2O dissociation energy barrier (Nd: 1.05 eV, Gd: 0.86 eV) compared with pure Pd (2.48 eV), suggesting that the introduction of the Nd_1Gd_1 can lower the H_2O dissociation energy barrier to promote the generation of reactive *H. More importantly, the Nd_1Gd_1 sites on Nd_1Gd_1Pd are more favorable to promote the H_2O dissociation compared to the energy barrier of H_2O dissociation of the Pd site (2.18 eV) on Nd_1Gd_1Pd. Combined with the adsorption energy data of H_2O on Nd_1Gd_1Pd with different sites (Supplementary Fig. 48), it can be speculated that the Nd_1Gd_1 on Nd_1Gd_1Pd not only serves as the effective H_2O adsorption sites but also as the main sites for the H_2O dissociation. Moreover, the effect of reactive *H toward HER at various sites of Nd_1Gd_1Pd was further investigated. Figure 6e, Supplementary

Fig. 52, and Supplementary Table 12 display that the value of hydrogen adsorption free energy (ΔG_{*H} = 2.90 eV) for Gd/Nd_1Gd_1Pd is far away from the optimal criteria (ΔG_{*H} = 0 eV) compared to that of pure Pd (ΔG_{*H} = −1.18 eV), whereas the value of ΔG_{*H} for Nd/Nd_1Gd_1Pd (ΔG_{*H} = 0.62 eV) is closer to the theoretical value compared to that of pure Pd, indicating that site balance effect of dual single-atom on the common hosts can achieve the inhibition of H_2 release process from Gd site, hence inhibiting the side-reaction HER activity, matching the comparison experimental results of the single-site samples and Nd_1Gd_1Pdene.

Combining the results from in situ FTIR and theoretical simulations, although Pd sites on Nd_1Gd_1Pd present an advantageous ΔG_{*H} of 0.35 eV, Pd sites on Nd_1Gd_1Pd are the main adsorption sites for reactant MBY rather than the main active sites for H_2O adsorption and dissociation, thus it is difficult for the HER process to be undertaken by the Pd sites on Nd_1Gd_1Pd. Besides, based on the ΔG_{*H} curves and in-situ FTIR test results of Nd_1Gd_1Pdene, the *H adsorption energy on the Nd_1Gd_1 site of Nd_1Gd_1Pd is weak compared to that of the Pd site of Nd_1Gd_1Pd (Fig. 6e). Nevertheless, the Pd-H signal (≈1992 cm^{-1}) was detected by the in situ FTIR test (Fig. 6c), indicating that the difference in *H adsorption energy between the Nd_1Gd_1 and Pd host induces a dual H-spillover effect at Nd_1Gd_1 sites, resulting in a rapid spillover of reactive *H produced by the Nd_1Gd_1 site to Pd site for MBY hydrogenation. A similar phenomenon (Pd–D, ≈1450 cm^{-1}) is also demonstrated when using D_2O as the proton source (Supplementary Fig. 53)[42]. Notably, in contrast to the Nd_1Gd_1Pdene, no significant Pd-H signal is observed on Pdene (Supplementary Fig. 54). This originates from the limited H_2O dissociation ability of Pd and the rapid consumption of *H during MBY hydrogenation, resulting in limited active *H supply[43]. In comparison, the introduction of Nd_1Gd_1 sites promotes H_2O dissociation on Nd_1Gd_1Pdene to increase the *H formation, and the *H is transferred to the Pd site via a dual H-spillover effect, which is beneficial for achieving the flow of reactive *H on the surface of Pd hosts to form a "hydrogen pool" for effective hydrogen supply and maximizing the use of reactive *H during MBY hydrotreating process[6].

The free energy profiles of *H adsorption at different sites on Nd_1Gd_1Pd prove the dual H-spillover pathway (Fig. 6f, g, and Supplementary Table 13). The H-spillover energy barriers (Nd → Pd: −0.27 eV, Gd → Pd: −2.55 eV) of Nd_1Gd_1 sites on Nd_1Gd_1Pd are lower than the *H desorption energy barriers (Nd: 0.62 eV, Gd: 2.90 eV), which suggests that the generated reactive *H at Nd_1Gd_1 sites prefers to transfer rapidly to the Pd sites for hydrogenation reaction via the dual H-spillover pathway rather than to form H_2 through the desorption process of *H[6]. A plausible reaction mechanism is speculated for MBY electrocatalytic semi-hydrogenation to MB and simultaneous production of high-purity $Mg(OH)_2$ (Fig. 6h). Taken together, the green synthesis of high-purity MBE and $Mg(OH)_2$ is achieved in seawater medium through H_2O dissociation step ($H_2O \rightarrow {}^*H + 2OH^-$), MBY semi-hydrogenation step (MBY + *H → *MBYH, *MBYH + *H → MBE), and Mg^{2+} precipitation step ($Mg^{2+} + 2OH^- \rightarrow Mg(OH)_2$).

In summary, we reported the synthesis of a Nd_1Gd_1Pdene DSAA catalyst for efficient MBY ECSH and high-purity $Mg(OH)_2$ production in the constructed natural seawater electrolysis system. The selectivity and FE for MBE of Nd_1Gd_1Pdene are as high as 96.7 and 87.3% under a high current density of −150 mA cm^{-2}, respectively, indicating the high activity and selectivity for the conversion of MBY to MBE, and the high-purity $Mg(OH)_2$ is simultaneously generated at the cathode. Meanwhile, the stability of >300 h on Nd_1Gd_1Pdene is achieved in the constructed MEA devices, revealing the long-term stability and practical viability towards industrial-level co-electrosynthesis of alkenol and $Mg(OH)_2$ from seawater. TEA further indicates that the projected revenue for per ton of MBE produced by this system is at least $8499, indicating a favorable economic potential compared with the conventional alkaline system. In situ FTIR and DFT calculations further suggest the dual hydrogen-spillover effect and synergistic co-catalytic effect induced by the interaction of the Nd_1Gd_1 site with Pd host, which is beneficial for promoting the spillover of dissociated reactive *H from Nd/Pd as an effective H_2O dissociation site to Pd host, resulting in the circulation of reactive *H on the surface to promote the MBY hydrogenation process and weakening the *H desorption to inhibit HER. This work provides a promising ECSH route for the simultaneous production of alkenols and $Mg(OH)_2$ in seawater, and offers a catalyst design strategy that leverages the atomic-level dual hydrogen-spillover effect to optimize ECSH performance.

Methods

Materials and chemicals

2-methyl-3-butyn-2-ol (C_5H_8O, MBY, 98%), 2-methyl-3-buten-2-ol ($C_5H_{10}O$, MBE, 98%), 2-methyl-2-butanol ($C_5H_{12}O$, MBA, 98%) and diethylenetriamine (DETA, AR, 99%) were purchased by Shanghai Macklin Biochemical Co., Ltd. (China). Palladium(II) acetylacetonate ($Pd(acac)_2$, 99%), neodymium(III) acetate hydrate ($Nd(C_5H_7O_2)_3{\cdot}xH_2O$, ≥99.9%), gadolinium(III) acetylacetonate hydrate ($Gd(C_5H_7O_2)_3{\cdot}xH_2O$, 99.9%), neodymium oxide (Nd_2O_3, ≥99.9%), gadolinium oxide (Gd_2O_3), N,N-dimethylformamide (DMF, AR, 99.5%), ethylene glycol (EG, AR, 98%), potassium hydroxide (KOH, AR, 85%), sodium hydroxide (NaOH, AR, ≥96%), sodium chloride (NaCl, AR, ≥99.5%), dichloromethane (DCM, ≥99.9%), 5,5-dimethyl-1-pyrroline N-oxide (DMPO, ≥97%), Nafion (5 wt %), and Nafion-N117 membrane were ordered from Aladdin Industrial Corporation (China). Acetone, sulfuric acid (H_2SO_4, ACS, 95.0–98.0%), hydrogen peroxide (H_2O_2, 35%) and ethanol (C_2H_5OH, AR, ≥95%) were provided from Shanghai Lingfeng Chemical Reagent Co., Ltd. (China). High-purity Ar gas (99.99%) was acquired from Hangzhou Special Gases Co., Ltd. (China). The seawater utilized in this work was acquired from the Yellow Sea (Qingdao, China). Ni foam (NF, 1.6 mm thick, >99.9%) and commercial IrO_2/Ti (20% IrO_2) were provided from Changsha Lyrun Material Co., Ltd.

Synthesis of Nd_1Gd_1Pdene

In a typical synthesis of Nd_1Gd_1Pdene, 1 g of KOH was completely dissolved in a 30 mL centrifuge tube with 6 mL of DMF and 4 mL of EG. Subsequently, 15 mg of $Pd(acac)_2$, 5 mg of $Nd(acac)_3{\cdot}xH_2O$, 5 mg of $Gd(acac)_3{\cdot}xH_2O$, and 10 mL of DETA were added into the above solution to form a homogeneous solution through sonication. The obtained solution was placed into a 50 mL Teflon-lined autoclave and maintained at 200 °C for 12 h. After the completed reaction was cooled down to room temperature (25 °C), the sample was collected by washing alternately with ethanol/water using centrifugation. Finally, the sample was dried in a vacuum oven (50 °C) for further characterization and testing.

Synthesis of Ln_1Pdene (M=Nd, Gd) and Pdene

Referring to the typical synthesis method of Nd_1Gd_1Pdene for preparing Ln_1Pdene, only $Nd(acac)_3{\cdot}xH_2O$ or $Gd(acac)_3{\cdot}xH_2O$ served as the rare-earth metal precursor. Moreover, only $Pd(acac)_2$ served as the metal precursor for synthesizing Pdene under typical conditions.

Material characterizations

SEM characterization equipped with an energy dispersive X-ray spectroscopy (EDS) system was collected from a Zeiss Gemini 500, and an AFM image was collected from a Bruker Dimension ICON. TEM, HAADF-STEM, EDS mapping data, and SAED were characterized through an FEI Tecnai G2 F30 with an accelerating voltage of 300 kV. Spherical aberration-corrected HADDF-STEM (AC-HAADF-STEM) characterization and electron energy loss spectroscopy (EELS) measurements were performed utilizing a FEI Titan Cubed Themis G2 300. XPS data were acquired through a PHI-5000versaprobeIII and XRD data were acquired from a PANalytical Empyrean powder diffractometer using Cu Kα radiation (λ = 0.1541 nm). ICP-OES (PerkinElmer 8300) data were employed to investigate the elemental

content of the sample. Ion chromatography (IC) was performed on the ICS-1100 to analyse electrolyte composition. X-ray absorption near-edge structure (XANES) and X-ray absorption fine structure (EXAFS) data were investigated utilizing the BL14W1 beamlines at the Shanghai Synchrotron Radiation Facility (Shanghai, China). The electrochemical in situ FTIR measurements were carried out on a Nicolet iS50 spectrometer equipped with MCT detector cooled by liquid nitrogen. Gas chromatography (GC) data were acquired from an Agilent 8890/7000D. NMR spectra tests were recorded through a Bruker Avance NEO 600, and EPR measurements were carried out utilizing a Bruker EMXmicro.

Electrochemical experiments

All electrochemical measurements were recorded on a CHI760E electrochemical workstation (Shanghai Chenhua Instrument Corporation, China) employing a three-electrode flow cell system, in which a commercial IrO_2/Ti electrode and Hg/HgO electrode served as counter electrode and the reference electrode, respectively. The catalyst-covered carbon paper (CP, $1 \times 1\ cm^2$) served as the working electrode. For a typical working electrode, 10 mg of ground catalyst was dispersed in a mixed solution comprising 1.2 mL of water, 0.6 mL of ethanol, and 0.2 mL of Nafion (5 wt%) by sonication to configure a $5\ mg\ mL^{-1}$ of homogeneous catalyst ink. Subsequently, the resulting ink was coated on carbon paper (CP) and dried in a vacuum oven (60 °C) for preparing a working electrode, in which the catalyst was loaded with $0.5\ mg\ cm^{-2}$. In a typical direct seawater alkynol electrocatalytic semi-hydrogenation (ECSH) to alkenol and electrochemical extraction of $Mg(OH)_2$, electrochemical performance tests were investigated by employing a flow cell equipped with MEA separated by a cation exchange membrane (Nafion-N117, ≈183 μm), where the cathodic and anodic solutions were seawater or NaCl + 1 M MBY (50 mL) and 1 M NaOH (50 mL) electrolytes, respectively. The commercial Nafion-N117 membrane was pre-treated using a standard activation procedure. The membrane was sequentially heated at 80 °C for 1 h in each of the following solutions: 3 wt% H_2O_2, deionized (DI) water, and 0.5 M H_2SO_4. After each step, the membrane was thoroughly washed with DI water to remove residual reagents. Finally, the treated membrane was stored in DI water at room temperature (25 °C) until use. All electrolytes were freshly prepared prior to each electrochemical experiment and stored at room temperature (25 °C) before use. When the catholyte was seawater + 1 M MBY (pH = 7.85 ± 0.02) and the anolyte was 1 M NaOH (pH = 13.87 ± 0.02), the resistance of the electrochemical cell was determined to be 3.25 ± 0.5 Ω. When the catholyte was 0.5 M NaCl (pH = 7.11 ± 0.02), and the anolyte was 1 M NaOH (pH = 13.87 ± 0.02), the resistance of the electrochemical cell was determined to be 3.05 ± 0.5 Ω. The flow rates of the cathode and anode through the peristaltic pump were $50\ mL\ min^{-1}$ and $50\ mL\ min^{-1}$, respectively. Before the direct seawater alkynol electrocatalytic semi-hydrogenation test, the electrolytes were purified with Ar (99.99%) for 30 min in the cathode and anode chambers, respectively. The chronopotentiometry (v–t) tests were conducted at $-20\ mA\ cm^{-2}$ (≈−1.45 ± 0.03 V vs. Hg/HgO), $-50\ mA\ cm^{-2}$ (≈−1.68 ± 0.03 V vs. Hg/HgO), $-100\ mA\ cm^{-2}$ (≈−1.95 ± 0.05 V vs. Hg/HgO), $-150\ mA\ cm^{-2}$ (≈−2.45 ± 0.08 V vs. Hg/HgO), and $-200\ mA\ cm^{-2}$ (≈−2.95 ± 0.08 V vs. Hg/HgO). All polarization curves were collected at a scan rate of $5\ mV\ s^{-1}$, and the current densities were normalized to the geometric area of CP. CV tests were recorded in Ar-saturated 1 M NaOH + 1 M MBY and 1 M NaOH electrolytes. The resistance of the electrochemical cell was determined by electrochemical impedance spectroscopy (EIS) measurements. EIS tests were performed over the measurement range from 0.1 Hz to 100 kHz. The Hg/HgO reference electrode was calibrated in H_2-saturated electrolyte (1 M NaOH or seawater) using a Pt foil as the working electrode and a graphite rod as the counter electrode. CV was performed at a scan rate of $5\ mV\ s^{-1}$, and the potential at which the current crossed zero was taken as 0 V versus the reversible hydrogen electrode (RHE). All potentials were reported versus the Hg/HgO reference electrode without RHE conversion unless otherwise stated. Due to the dynamic fluctuations in local pH near the electrode surface during the seawater alkynol electrocatalytic semi-hydrogenation process, the potentials were not directly converted to the RHE scale. For comparison, the potentials can be converted to the RHE scale based on the initial bulk electrolyte pH using the following equation (1):

$$E(\text{vs.RHE}) = \text{E(vs.Hg/HgO)} + 0.098 + 0.059 \times \text{pH}(25\,^{\circ}\text{C}) \quad (1)$$

The electrochemically active surface area (ECSA) of the catalysts was qualitatively evaluated through testing the electrochemical double-layer capacitance (C_{dl}). CV tests were conducted in a non-faradaic potential region at scan rates ranging from 20 to $120\ mV\ s^{-1}$. The capacitive current density difference ($\Delta j = j_a - j_c$) at a selected potential was plotted as a function of the scan rate, where j_a and j_c represent the anodic and cathodic current densities, respectively. The C_{dl} value was obtained from the slope of the linear fitting according to the equation (2):

$$\Delta j = 2C_{dl} \times v \quad (2)$$

where v is the scan rate. The obtained C_{dl} values were used to qualitatively compare the relative ECSAs of the catalysts.

For the constructed MEA electrolyzer ($1 \times 1\ cm^2$ or $2 \times 2\ cm^2$) in a two-electrode configuration, catalyst-coated CP ($1 \times 1\ cm^2$ or $2 \times 2\ cm^2$) with a catalyst loading of $0.5\ mg\ cm^{-2}$ was used as the cathode, while NF or commercial IrO_2/Ti served as the anode. When the catholyte was seawater + 1 M MBY, and the anolyte was seawater (pH = 7.80 ± 0.3), the resistance of the electrochemical cell was determined to be 8.01 ± 0.3 Ω. When the catholyte was seawater + 1 M MBY, and the anolyte was 1 M NaOH, the resistance of the electrochemical cell was determined to be 3.9 ± 0.2 Ω. When the catholyte was seawater + 1 M MBY, and the anolyte was 1 M Na_2SO_4 (pH = 7.02 ± 0.03), the resistance of the electrochemical cell was determined to be 4.50 ± 0.2 Ω.

EPR experiments

Firstly, the electrocatalytic tests on Nd_1Gd_1Pdene were recorded in 0.5 M NaCl electrolytes with or without 1 M MBY at a current density of $-50\ mA\ cm^{-2}$ for 5 min. Thereafter, 0.8 mL of electrolytes were promptly extracted from two cathode chambers, and 25 mg of DMPO was added to the above electrolytes. Finally, the obtained solutions were subjected to EPR tests.

In situ FTIR experiments

In situ FTIR measurements were conducted using a Nicolet iS50 spectrometer, which was configured with a liquid nitrogen-cooled MCT detector. To prepare the reflective working electrode, a gold (Au) thin film (~60 nm) was chemically deposited onto a Si prism via a two-step wet process[44]. Prior to Au deposition, the Si prism underwent a rigorous cleaning protocol: the IR reflection surface was first polished using a diamond suspension, followed by ultrasonic cleaning in deionized water. The prism was then treated in a piranha solution (H_2SO_4: H_2O_2 = 7:3 by volume) for 2 h to ensure surface purity. For the working electrode, 30 μL of the prepared electrocatalyst ink was cast onto the Au-modified Si prism and dried. This assembly was integrated into a H-type electrolytic cell, where a Pt mesh (1 cm × 1 cm) and an Hg/HgO electrode served as the counter and reference electrodes, respectively. The electrolyte used was a 0.5 M NaCl solution containing 1 M MBY. Spectral acquisition and electrochemical experiments were conducted simultaneously. Firstly, the i–t method was conducted at a current density of $-50\ mA\ cm^{-2}$ in this experiment, with FTIR spectra recorded at specific intervals ranging from 200 to 1200 s. Secondly, the i–t method was conducted at a current density from −15 to $-150\ mA\ cm^{-2}$

in this experiment, capturing spectra corresponding to each current density. All FTIR data are presented as relative reflectance changes, defined by the following equation (3):

$$\Delta R/R = (E_S - E_R)/E_R \quad (3)$$

where E_S and E_R represent the sample and reference spectra, respectively. Unless otherwise noted, the spectral resolution for all measurements was set to 4 cm^{-1}.

Product analysis

The collected cathode electrolyte after the υ–t tests was directly analyzed by NMR spectroscopy, and the formed $Mg(OH)_2$ was acquired from the cathodic electrolyte via centrifugation. Also, for further investigating MBY conversion, MBE selectivity/FE, MBE production rate and by-product MBA selectivity/FE, the cathodic electrolyte was collected and extracted by using DCM. The extracted products were investigated by comparing the GC retention times and mass spectra. The MBY conversion, MBE selectivity/FE, MBE production rate and by-product MBA selectivity/FE were calculated by analyzing the GC results and according to the following equations (4), (5), (6), and (7)[3]:

$$\text{MBY conversion} = \frac{C_{MBY1} - C_{MBY}}{C_{MBY1}} \times 100\% \quad (4)$$

$$\text{MBE selectivity} = \frac{C_{MBE}}{C_{MBE} + C_{MBA}} \times 100\% \quad (5)$$

$$\text{MBA selectivity} = \frac{C_{MBA}}{C_{MBE} + C_{MBA}} \times 100\% \quad (6)$$

$$FE = \frac{N(\text{Production}) \times Z \times F}{Q} \times 100\% \quad (7)$$

Where C_{MBY1} is the initial MBY concentration, C_{MBY}, C_{MBE}, and C_{MBA} are the concentrations of MBY, MBE, MBA in the electrolyzed product, N is the molar amount for the formed MBE/MBA, Z is the number of electrons transferred for the formed MBE ($Z = 2$), MBA ($Z = 4$) and H_2 ($Z = 2$), F is the Faraday constant (96,485 C mol^{-1}), Q is the total amount of charge consumed.

Computational methods

According to the experiments and characterization results, Nd_1Gd_1Pdene possesses a typical single-phase fcc structure and single-atom alloy structure, and the atomic ratio for Pd/Nd/Gd on Nd_1Gd_1Pdene is approximately 8:1:1 according to ICP and SEM-EDS results. Thus, in the DFT simulation process, we constructed a $2 \times 2 \times 1$ supercell containing 48 atoms (Pd:38/Nd:5/Gd:5 ≈ Pd:8/Nd:1/Gd:1) using the fcc cubic phase of Pd as a template. All the DFT calculations were performed by using the VASP package[45]. The effect of water solvent was taken into account via the implicit solvation model implemented in the VASPsol package[46,47]. The RPBE functional with Becke-Johnson damping D3 dispersion correction was utilized[48,49]. The PAW method was employed to describe the core treatments of the atoms[50]. The kinetic energy of the wavefunctions were set as 500 eV. Periodic slabs with $4 \times 2\sqrt{3}$ supercell were applied to model the (111) surfaces. $2 \times 2 \times 1$ Monkhorst-Pack grids were implemented with $\sigma = 0.1$ eV of Gaussian smearing[51,52]. The distance between the top and the bottom of the adjacent slab was set to about 15 Å. The wavefunctions were fully relaxed until the electronic energy change and the change of eigenvalues were smaller than 10^{-5} eV. The structures were fully relaxed until the maximal force on each atom was less than 0.05 eV/Å. The CI-NEB method was used to determine the reaction pathway and energy barrier[53]. The adsorption energy (Eads) of adsorbate (MBY*, MBE*) was defined as (7):

$$E_{ads} = E_{Total} - E_{surf} - E_{adsorbate}(g) \quad (7)$$

where E_{total}, E_{surf}, and $E_{adsorbate}$ (g) are the energy of adsorbate adsorbed on the surface, the energy of clean surface, and the energy of an isolated molecule in a cubic periodic box, respectively.

The crystal structures were visualized using the VESTA software[54]. The atomic coordinates and optimized structures of calculation models are provided in Supplementary Data 1.

COMSOL Multiphysics simulation

The pH values for the electrolyte surrounding the electrode were simulated and calculated on COMSOL Multiphysics version 6.0 software[16].

Data availability

All data supporting the findings of this study are available within the article and its Supplementary Information. Source data are provided as a Source data file in the Supplementary Information. Source data are provided with this paper.

References

1. Bu, J. et al. Selective electrocatalytic semihydrogenation of acetylene impurities for the production of polymer-grade ethylene. *Nat. Catal.* **4**, 557–564 (2021).
2. Zhang, L. et al. Deprotonated 2-thiolimidazole serves as a metal-free electrocatalyst for selective acetylene hydrogenation. *Nat. Chem.* **16**, 893–900 (2024).
3. Bu, J. et al. Highly selective electrocatalytic alkynol semihydrogenation for continuous production of alkenols. *Nat. Commun.* **14**, 1533 (2023).
4. Gao, Y. et al. Electrocatalytic semi-hydrogenation of alkynes using water as the hydrogen source. *Nat. Protoc.* https://doi.org/10.1038/s41596-025-01230-z (2025).
5. Zhao, Y. et al. Dopant- and surfactant-tuned electrode-electrolyte interface enabling efficient alkynol semi-hydrogenation. *J. Am. Chem. Soc.* **145**, 6516–6525 (2023).
6. Tan, Q. et al. Tandem electrocatalytic alkyne semihydrogenation over bicomponent catalysts through hydrogen spillover. *Angew. Chem. Int. Ed.* **63**, e202400483 (2024).
7. Li, S. et al. Green electrosynthesis of hydroxylamines via CuS suppressing N horizontal line O bond cleavage. *Angew. Chem. Int. Ed.* **64**, e202507853 (2025).
8. Zhu, K. et al. Unraveling the role of interfacial water structure in electrochemical semihydrogenation of alkynes. *ACS Catal.* **12**, 4840–4847 (2022).
9. Liu, C., Chen, F., Zhao, B. H., Wu, Y. & Zhang, B. Electrochemical hydrogenation and oxidation of organic species involving water. *Nat. Rev. Chem.* **8**, 277–293 (2024).
10. Fan, R. et al. Ultrastable electrocatalytic seawater splitting at ampere-level current density. *Nat. Sustain.* **7**, 158–167 (2024).
11. Chen, L. et al. Seawater electrolysis for fuels and chemicals production: fundamentals, achievements, and perspectives. *Chem. Soc. Rev.* **53**, 7455–7488 (2024).
12. Cai, L. et al. Atomically asymmetrical Ir-O-Co sites enable efficient chloride-mediated ethylene electrooxidation in neutral seawater. *Angew. Chem. Int. Ed.* **64**, e202417092 (2025).
13. Huang, L., Bao, D., Jiang, Y., Zheng, Y. & Qiao, S. Z. Electrocatalytic acetylene hydrogenation in concentrated seawater at industrial current densities. *Angew. Chem. Int. Ed.* **63**, e202405943 (2024).
14. Huang, L. et al. Ethylene electrooxidation to 2-chloroethanol in acidic seawater with natural chloride participation. *J. Am. Chem. Soc.* **145**, 15565–15571 (2023).

15. Yi, L. et al. Supersolidophobic Pt catalyst for long-term natural seawater electrolysis with hydrogen production and magnesium extraction. *Nat. Commun.* **16**, 11493 (2025).
16. Yi, L. et al. Solidophobic surface for electrochemical extraction of high-valued $Mg(OH)_2$ coupled with H_2 production from seawater. *Nano Lett.* **24**, 5920–5928 (2024).
17. Liang, J. et al. Electroreduction of alkaline/natural seawater: self-cleaning Pt/carbon cathode and on-site co-synthesis of H_2 and Mg hydroxide nanoflakes. *Chem* **10**, 3067–3087 (2024).
18. Yong, M. et al. Sustainable lithium extraction and magnesium hydroxide co-production from salt-lake brines. *Nat. Sustain.* **7**, 1662–1671 (2024).
19. Kang, J. et al. Interfacial asymmetrically coordinated Zn-MOF for high-efficiency electrosynthetic oxime. *Angew. Chem. Int. Ed.* **64**, e202419550 (2025).
20. Deng, K. et al. Breaking the energy linear relationships between C identical with C and C horizontal line C bonds over porous intermetallic Pd_2Ga metallene boosting alkynol semihydrogenation. *ACS Nano* **20**, 2311–2322 (2026).
21. Mao, Q. et al. Atomically dispersed Cu coordinated Rh metallene arrays for simultaneously electrochemical aniline synthesis and biomass upgrading. *Nat. Commun.* **14**, 5679 (2023).
22. Liao, P. et al. Cu-Bi bimetallic catalysts derived from metal-organic framework arrays on copper foam for efficient glycine electrosynthesis. *Angew. Chem. Int. Ed.* **64**, e202417130 (2025).
23. Barraza-Fierro, J. I. et al. Modeling electrochemical impedance spectroscopy results of Cu and Cu-thiosemicarbizide-boron nitride nanosheets electrodes in 3.5 wt% NaCl solution, based on an electrochemical reaction mechanism. *Crystals* **13**, 809 (2023).
24. Sha, Q. et al. 10,000-h-stable intermittent alkaline seawater electrolysis. *Nature* **639**, 360–367 (2025).
25. Yang, J. Y. et al. Electrochemical corrosion resistance of the amorphous and crystalline Pd-based alloys in simulated seawater. *Mater. Corros.* **69**, 1509–1515 (2018).
26. Mezger, R. P., Vrijhoef, M. M. A. & Greener, E. H. Corrosion resistance of three high-palladium alloys. *Dent. Mater.* **1**, 177–179 (1985).
27. Prabhu, P. & Lee, J. M. Metallenes as functional materials in electrocatalysis. *Chem. Soc. Rev.* **50**, 6700–6719 (2021).
28. Zhou, C. et al. Oxophilic gallium single atoms bridged ruthenium clusters for practical anion-exchange membrane electrolyzer. *Nat. Commun.* **15**, 6741 (2024).
29. Li, P., Qi, Z. & Yan, D. Rare earth Er-Nd dual single-atomic catalysts for efficient visible-light induced CO_2 reduction to $C_nH_{2n+1}OH$ (n=1, 2). *Angew. Chem. Int. Ed.* **63**, e202411000 (2024).
30. Feng, J. et al. Improving CO_2-to-C_{2+} product electroreduction efficiency via atomic lanthanide dopant-induced tensile-strained CuO_x Catalysts. *J. Am. Chem. Soc.* **145**, 9857–9866 (2023).
31. Deng, K. et al. Hydrogen spillover effect tuning the rate-determining step of hydrogen evolution over Pd/Ir heterometallene for industry-level current density. *Appl. Catal. B Environ. Energy* **352**, 124047 (2024).
32. Zhou, Y. et al. Alternating pulse driven periodic reactivation of high-entropy mesoporous film boosts continuous membrane-free PET waste upcycling coupled with H_2 production. *Adv. Funct. Mater.* **36**, e11835 (2025).
33. Chen, L. et al. Promoting electrocatalytic methanol oxidation of platinum nanoparticles by cerium modification. *Nano Energy* **73**, 104784 (2020).
34. Hu, J. et al. Neodymium-doped IrO_2 electrocatalysts supported on titanium plates for enhanced chlorine evolution reaction performance. *ChemElectroChem* **8**, 1204–1210 (2021).
35. Wang, X. et al. Embedding oxophilic rare-earth single atom in platinum nanoclusters for efficient hydrogen electro-oxidation. *Nat. Commun.* **14**, 3767 (2023).
36. Li, A. et al. Atomically dispersed hexavalent iridium oxide from MnO_2 reduction for oxygen evolution catalysis. *Science* **384**, 666–670 (2024).
37. Poerwoprajitno, A. R. et al. A single-Pt-atom-on-Ru-nanoparticle electrocatalyst for CO-resilient methanol oxidation. *Nat. Catal.* **5**, 231–237 (2022).
38. Li, J. et al. Sustainable oxime production via the electrosynthesis of hydroxylamine in a free state. *Nat. Synth.* **4**, 1598–1609 (2025).
39. Xian, J. et al. Electrocatalytic synthesis of essential amino acids from nitric oxide using atomically dispersed Fe on N-doped carbon. *Angew. Chem. Int. Ed.* **62**, e202304007 (2023).
40. Guan, S., Attard, G. A. & Wain, A. J. Observation of substituent effects in the electrochemical adsorption and hydrogenation of alkynes on Pt{*hkl*} using SHINERS. *ACS Catal.* **10**, 10999–11010 (2020).
41. Fan, C. et al. Neodymium-evoked valence electronic modulation to balance reversible oxygen electrocatalysis. *Adv. Energy Mater.* **13**, 2203244 (2022).
42. Kondo, J. N. et al. Pd–H species on electrode stabilized by solvent co-adsorption: observation by operando IR spectroscopy. *J. Phys. Chem. C* **126**, 19376–19385 (2022).
43. Zhao, R. et al. Pd single atoms guided proton transfer along an interfacial hydrogen bond network for efficient electrochemical hydrogenation. *Sci. Adv.* **11**, eadu1602 (2025).
44. Yan, Y. et al. Nonredox trivalent nickel catalyzing nucleophilic electrooxidation of organics. *Nat. Commun.* **14**, 7987 (2023).
45. Kresse, G. & Furthmuller, J. Efficiency of ab-initio total energy calculations for metals and semiconductors using a plane-wave basis set. *Comput. Mater. Sci.* **6**, 15–50 (1996).
46. Gauthier, J. A. et al. Unified approach to implicit and explicit solvent simulations of electrochemical reaction energetics. *J. Chem. Theory Comput.* **15**, 6895–6906 (2019).
47. Mathew, K., Sundararaman, R., Letchworth-Weaver, K., Arias, T. A. & Hennig, R. G. Implicit solvation model for density-functional study of nanocrystal surfaces and reaction pathways. *J. Chem. Phys.* **140**, 084106 (2014).
48. Kresse, G. & Joubert, D. From ultrasoft pseudopotentials to the projector augmented-wave method. *Phys. Rev. B* **59**, 1758–1775 (1999).
49. Grimme, S., Antony, J., Ehrlich, S. & Krieg, H. A consistent and accurate ab initio parametrization of density functional dispersion correction (DFT-D) for the 94 elements H-Pu. *J. Chem. Phys.* **132**, 154104 (2010).
50. Hammer, B., Hansen, L. B. & Nørskov, J. K. Improved adsorption energetics within density-functional theory using revised Perdew-Burke-Ernzerhof functionals. *Phys. Rev. B* **59**, 7413–7421 (1999).
51. Monkhorst, H. J. & Pack, J. D. Special points for Brillouin-zone integrations. *Phys. Rev. B* **13**, 5188–5192 (1976).
52. Ho, K. M., Fu, C. L., Harmon, B. N., Weber, W. & Hamann, D. R. Vibrational frequencies and structural properties of transition metals via total-energy calculations. *Phys. Rev. Lett.* **49**, 673–676 (1982).
53. Henkelman, G., Uberuaga, B. P. & Jónsson, H. A climbing image nudged elastic band method for finding saddle points and minimum energy paths. *J. Chem. Phys.* **113**, 9901–9904 (2000).
54. Momma, K. & Izumi, F. VESTA 3 for three-dimensional visualization of crystal, volumetric and morphology data. *J. Appl. Crystallogr.* **44**, 1272–1276 (2011).

Acknowledgements

This research was supported by the Zhejiang Provincial Natural Science Foundation of China under grant no. LR24B060001 (H.J.W.), and National Natural Science Foundation of China under grant no. 22572173 (L.W.), 22478345 (H.J.W.). Crystal structure visualizations were generated using the VESTA software.

Author contributions

H.J.W., L.W., and Q.M. conceived the idea and designed the experiments. H.J.W., L.W. supervised the project. Q.M., W.X.W., and R.Y. carried out catalyst synthesis and electrochemical experiments. K.D., H.J.Y. performed structural characterizations and analyzed XANES and EXAFS data. R.Y. performed and analyzed DFT calculations. Q.M., W.X.W., and R.Y. conducted in situ FTIR and EPR measurements. H.J.W., L.W., and Q.M. analyzed the results and wrote the paper. W.Z.L., S.G. helped with the revision of the paper. All authors discussed the results and commented on the manuscript.

Competing interests

The authors declare no competing interests.

Additional information

Supplementary information The online version contains Supplementary material available at https://doi.org/10.1038/s41467-026-71588-5.

Correspondence and requests for materials should be addressed to Wenzhen Li, Liang Wang, Hongjing Wang or Shaojun Guo.

Peer review information *Nature Communications* thanks Nikolay Kornienko, Sang Uck Lee, Guangqin Li and the other anonymous reviewer(s) for their contribution to the peer review of this work. A peer review file is available.